Slender wing beam reduction method for gradient-based aeroelastic design optimization

O. Stodieck*, J. E. Cooper†, S. A. Neild‡, M. H. Lowenberg§
Department of Aerospace Engineering, University of Bristol, Bristol BS8 1TR, U.K.

L. Iorga¶
Airbus Operations Ltd., Pegasus House, Aerospace Avenue, Bristol BS34 7PA, U.K.

The efficiency and scope of aeroelastic wing optimization strategies can be increased using analysis-specific structural idealizations, such as high-fidelity models for detailed stress analyses and low-fidelity models for aeroelastic analyses. In this work, a numerical method is presented that enables efficient and accurate reduction of a high-fidelity finite element model to a Timoshenko beam-based model with lumped masses. The result is a representation based on 13 independent physical beam stiffness parameters per element. The method also yields analytical beam sensitivities with respect to changes in the high-fidelity model. Using these, an approach is suggested for integrating the beam reduction method into a gradient-based multidisciplinary design optimization architecture. The reduction technique is demonstrated on a simplified wing-box and on the University of Bristol Ultra-Green aircraft configuration wing. The effects of unbalanced skin composite laminates, rotated internal ribs, varying wing taper and sweep, and wing boundary constraints on the wing stiffness are shown to be captured with sufficient accuracy for static and dynamic aeroelastic analysis purposes. The accuracy of the analytically calculated gradients is demonstrated by comparison with complex-step and finite difference derivative approximations.

Nomenclature

A, B	=	beam element inboard and outboard nodes respectively
$\bar{\bar{A}}$	=	equivalent beam section area along the elastic axis (m^2)
$[C], [\bar{C}], [\bar{\bar{C}}], [\bar{\bar{C}}_p]$	=	beam element flexibility matrices in corresponding coordinate systems
D	=	distance between node B and the node where the static forces F_2 and F_3 are applied (m)
E, G	=	material Young's modulus and shear modulus (Pa)

*Aerospace Engineering Research Associate
†Royal Academy of Engineering Airbus Sir George White Professor of Aerospace Engineering, FAIAA
‡Professor of Nonlinear Structural Dynamics
§Professor of Flight Dynamics
¶Optimization Engineer

$\boldsymbol{F}, \bar{\bar{\boldsymbol{F}}}$	=	vector of applied forces and moments in the $[x, y, z]$ and $[\bar{\bar{x}}, \bar{\bar{y}}, \bar{\bar{z}}]$ directions respectively (N, Nm)
$\boldsymbol{g}$	=	vector of optimization objective and constraint function values
h	=	complex-step derivative approximation step size
I_1, I_2, I_{12}, J	=	beam bending and torsion stiffness parameters in the $[x, y, z]$ directions (m^4)
$\bar{\bar{I}}_1, \bar{\bar{I}}_2, \bar{\bar{I}}_{12}, \bar{\bar{J}}$	=	beam bending and torsion stiffness parameters in the $[\bar{\bar{x}}, \bar{\bar{y}}, \bar{\bar{z}}]$ directions (m^4)
$\bar{\bar{k}}_y, \bar{\bar{k}}_z$	=	Timoshenko beam theory shear coefficients in the $[\bar{\bar{y}}, \bar{\bar{z}}]$ directions
$I_{XYZ,XYZ}$	=	beam model lumped mass element inertia terms (kgm^2)
K_1, K_2	=	beam bending-torsion stiffness coupling parameters in the $[x, y, z]$ directions (Nm^2)
$[K]$	=	beam element stiffness matrix in the $[x, y, z]$ directions
l_{AB}	=	length of the beam element between nodes A and B (m)
$\boldsymbol{L}$	=	vector external loads (N,Nm)
L_{AB}	=	length of the elastic axis between nodes SC_A and SC_B (m)
m_i	=	single GFEM element mass (kg)
m_s	=	mass of a beam model lumped mass element (kg)
$[M]$	=	mass matrix
$\bar{\bar{N}}_y, \bar{\bar{N}}_z$	=	centroid offsets from the elastic axis in the $[\bar{\bar{y}}, \bar{\bar{z}}]$ directions (m)
$\bar{\bar{N}}_{yp}, \bar{\bar{N}}_{zp}$	=	centroid offsets from the elastic axis in the principal axes directions (m)
$\boldsymbol{p}$	=	beam element orientation vector in the $\bar{\bar{x}}\bar{\bar{y}}$-plane
$\boldsymbol{q}$	=	shortest vector from node B to the element elastic axis
$\boldsymbol{Q}$	=	beam flexibility equation coefficient denominator ($[Nm^2]^3$)
$SC_A, \boldsymbol{SC_A}$	=	beam element inboard shear center and offset vector from node A, $\boldsymbol{SC_A} = [0, SC_{Ay}, SC_{Az}]^T$ (m)
$SC_B, \boldsymbol{SC_B}$	=	beam element outboard shear center and offset vector from node B, $\boldsymbol{SC_B} = [0, SC_{By}, SC_{Bz}]^T$ (m)
$[T], [T_1]$	=	rotation matrix from $[x, y, z]$ to $[\bar{x}, \bar{y}, \bar{z}]$ and from $[\bar{x}, \bar{y}, \bar{z}]$ to $[\bar{\bar{x}}, \bar{\bar{y}}, \bar{\bar{z}}]$ directions respectively
$[T_p]$	=	rotation matrix from the $[\bar{\bar{x}}, \bar{\bar{y}}, \bar{\bar{z}}]$ to the principal axes directions
$\boldsymbol{u}$	=	vector from SC_B to node B, defined in the $[\bar{\bar{x}}, \bar{\bar{y}}, \bar{\bar{z}}]$ directions
$\boldsymbol{U}$	=	vector of reference node displacements and rotations in the x, y, z directions (m, rad)
$\boldsymbol{\Delta U}, \boldsymbol{\Delta \bar{\bar{U}}}$	=	vectors of relative displacements and rotations of node B wrt. node A (m, rad)
$\boldsymbol{v}$	=	vector of global finite element model design variables
$\boldsymbol{w}$	=	vector from the centroid to node B, defined in the $[\bar{\bar{x}}, \bar{\bar{y}}, \bar{\bar{z}}]$ directions
x, y, z	=	local beam reference axis coordinate system, with $\vec{x} = \overrightarrow{AB}$ (LCS)
$\bar{\bar{x}}, \bar{\bar{y}}, \bar{\bar{z}}$	=	rotated elastic axis coordinate system, with $\vec{\bar{\bar{x}}} = \overrightarrow{SC_A SC_B}$ (RLCS)
X, Y, Z	=	global model analysis coordinate system directions

$[X, Y, Z]_i$ = vector from the beam reference node to the GFEM element 'i' centroid in the $[X, Y, Z]$ directions (m)

$[X, Y, Z]_{CG}$ = vector from the beam reference node to the lumped mass element in the $[X, Y, Z]$ directions (m)

$\alpha'_x, \delta''_y, \delta''_z$ = beam twist rate along the x-direction and curvatures in the y and z directions (rad/m, m^{-1})

$\gamma_y, \gamma_z, \gamma'_y$ = extrinsic and intrinsic rotation angles of the elastic axis with respect to the x-direction (rad)

$\bar{\gamma}_x, \bar{\gamma_{xp}}$ = rotation angles about the elastic axis associated with transformation matrices $[T_1]$ and $[T_p]$ (rad)

$\bar{\bar{\delta}}_y, \bar{\bar{\delta}}_z$ = bending related deflections in the $[\bar{\bar{y}}, \bar{\bar{z}}]$ directions (m)

Ψ_1, Ψ_2 = non-dimensional bend-twist coupling parameters

$\mathbf{\Omega}$ = vector of beam element stiffness parameters

I. Introduction

The use of multidisciplinary design optimization (MDO) tools for the preliminary design of aircraft structures can lead to significant aircraft performance improvements. For example, it allows unconventional configurations and materials to be explored in a systematic way, while satisfying a wide range of constraints. One application of MDO is the design of aerostructures subject to aerodynamic, stress and aeroelastic constraints. Existing wing MDO implementations, such as those described in [1–6], tend to use three-dimensional global finite element models (GFEMs) of wing structures for stress and aeroelastic analyses, where the wing components (spars, skins, ribs and stringers) are modeled using discrete shell and beam elements. In such studies, the structural model refinement is mainly driven by the choice of structural optimization variables and stress constraints, leading to models with 10^4 to 10^6 degrees of freedom. Structural optimization variables include the wing component thicknesses and material properties, but also the locations and orientations of ribs, spars and stringers within the wing. Stress constraints are related to component strength and buckling reserve factors, which are functions of the internal wing loads calculated using the GFEM. However, generally, stress analysis only needs to be performed for a small number of critical load cases which define the maximum/minimum external load envelope. Since the critical cases are not known a priori, static and dynamic aeroelastic analyses have to be performed for many different flight and ground cases (100,000 cases or more [7]) to calculate the external aerodynamic and inertial loads. For these aeroelastic analyses, it is arguably sufficient to retain a reduced number of degrees of freedom along the wing span, so that the wing bending and torsion behaviors are captured with sufficient accuracy, whilst minimizing computational costs. Management of the computational costs is important for MDO purposes, despite the increasing capabilities of high performance computing hardware, since the aeroelastic analyses are repeated for every design iteration during the optimization process. In addition, these costs could increase significantly if nonlinear aeroelastic analyses had to be performed within the optimization to capture geometric and aerodynamic nonlinearities, such as those occurring on highly flexible wings [8, 9]. Therefore, by using a single structural wing idealization for both the stress and the aeroelastic analyses, current wing MDO tools implicitly make a compromise either between

the calculated stress fidelity and the aeroelastic analysis efficiency, or on the number of aeroelastic load cases that can realistically be considered within the design optimization process.

As a result, there is a strong argument to be made in favor of developing an integrated, multi-fidelity analysis and optimization architecture, where the structural optimization variables are defined with respect to a GFEM model, which is also used for stress analysis purposes, but where the wing is modeled as a beam for aeroelastic analysis purposes. A key requirement for such an approach is an efficient, yet sufficiently accurate, means of reducing a GFEM to a beam model in an automated fashion. In practice, two different types of methods may be used to calculate equivalent beam stiffness properties. In one approach, equivalent beam properties are determined directly from detailed descriptions of the wing section geometries and material properties along the wing span. Implementations include the variational asymptotic beam sectional analysis (VABS) [10] and other methods that use thin-walled beam assumptions, as reviewed in [11, 12]. Higher-order one-dimensional element formulations for composite structures have also been proposed by Carrera and Petrolo [13]. These studies, and those they reference, show that sectional out-of-plane warping and shear flexibility effects can be captured accurately for anisotropic, geometrically complex beam sections. These methods have been successfully used in preliminary design studies and even integrated into MDO architectures [14, 15]. However, sectional analysis methods become impractical for wings with numerous section variations due to local cut-outs, reinforcements or section shape changes. Neither the effects of internal ribs, nor the effects of misalignments between the beam reference axis and internal stringers or spars can be formally captured using a single beam section. Furthermore, section properties may have to be extracted manually from the GFEM model if no separate structural description, such as geometric design data, is available.

In the second type of method, the beam properties are calculated numerically, via a small number of static simulations of the full fidelity GFEM. Identification procedures are used to determine beam properties yielding equivalent displacement responses to the full model. This approach was recently implemented in [6], to assess the effects of different spar and rib layouts on Euler-Bernoulli beam bending and torsion parameters. SwiftComp, an implementations of the mechanics of structural genome (MSG) theory developed by Yu [16], also uses this approach for the multi-scale modeling of heterogeneous composite structures, which cannot currently be handled by sectional analysis methods. Another implementation is the blade (or beam) property extraction method (BPE) developed by Malcolm and Laird [17]. BPE has been used to generate accurate wind-turbine blade models for aeroelastic analyses from existing GFEM models. In addition to being numerically efficient, the most notable benefit of this type of method is that no information is required about the wing or blade sectional properties to perform the beam reduction. It is therefore possible to reduce wings with cut-outs, discrete structural features or varying spar, stringer or rib orientations to accurate beam models. Given the requirements listed above, this type of method seems naturally more appropriate for rapid aeroelastic wing optimization, and it is selected to form the basis of the current work.

Moreover, MDO architectures with numerous design variables and constraints use gradient-based optimization

algorithms to ensure convergence towards optimal solutions, with [18] providing a survey of different architectures. The load and constraint sensitivities from the aeroelastic beam model analyses can be integrated in a gradient based MDO architecture using a gradient chain-ruling approach, provided that the beam model sensitivities with respect to changes in the GFEM design variables are available. For best efficiency and accuracy, the beam model gradients should be calculated analytically.

The objective of this paper is to present a beam reduction method, which satisfies the efficiency, accuracy and gradient output requirements listed above, and which has, therefore, been specifically developed for rapid aeroelastic design optimization with detailed stress constraints. The improved method has been realized by, firstly, extending the BPE method to yield a set of 13 independent physical beam properties, based on Timoshenko beam theory with isotropic material properties, from any fully coupled 6x6 stiffness matrix. The calculation of equivalent Timoshenko beam properties allows the equivalent beam models to be analyzed using standard FEM solvers and element types. This is achieved while retaining a key advantage of the BPE method, which is that the GFEM description is only required within the FEM analysis code, and so the reduction method is decoupled from the definition of the structural box geometry and material properties. Secondly, the method allows beam stiffness sensitivities, due to changes in the GFEM variables, to be derived analytically from the displacements sensitivities of the GFEM in a computationally efficient manner. Integration of the proposed beam reduction method into a gradient-based MDO architecture is discussed in section II, followed by a description of the method itself in sections III and IV, which outline the equivalent beam stiffness and mass calculations respectively. The method is then demonstrated on a simplified wing box configuration and also on the University of Bristol ultra-green (BUG) wing GFEM (section V). These models are representative of the type of wing GFEMs used in industry, which include discrete geometric features, variable section geometries and anisotropic material properties. Finally, the method for extraction of gradient data is described in section VI, with an example discussed in section VII. All analyses are performed using MSC Nastran, however, the technique is equally applicable to other solvers using a similar finite element formulation.

II. Aeroelastic design optimization

In this section, as a motivation for the development of the beam reduction method presented here, we illustrate how the method could be integrated into a gradient-based MDO tool. For this purpose, a monolithic multidisciplinary feasible (MDF) MDO architecture [18] is considered, since it provides a simple optimization problem description and relates to a number of other MDO architectures used in the literature. MDF requires a full multidisciplinary analysis to be performed within each optimization iteration, as shown in Fig. 1, where model analyses are shown in rectangles and input/output data is shown in parallelograms. The multidisciplinary analysis starts with an update of design variable values $\boldsymbol{v}$ in the GFEM model (1). Then, the GFEM to beam reduction is performed (2), triggering an update of the beam model (3) and yielding the gradients of beam model properties to optimization variables $\partial\Omega/\partial v$ and $\partial M/\partial v$ (4). For

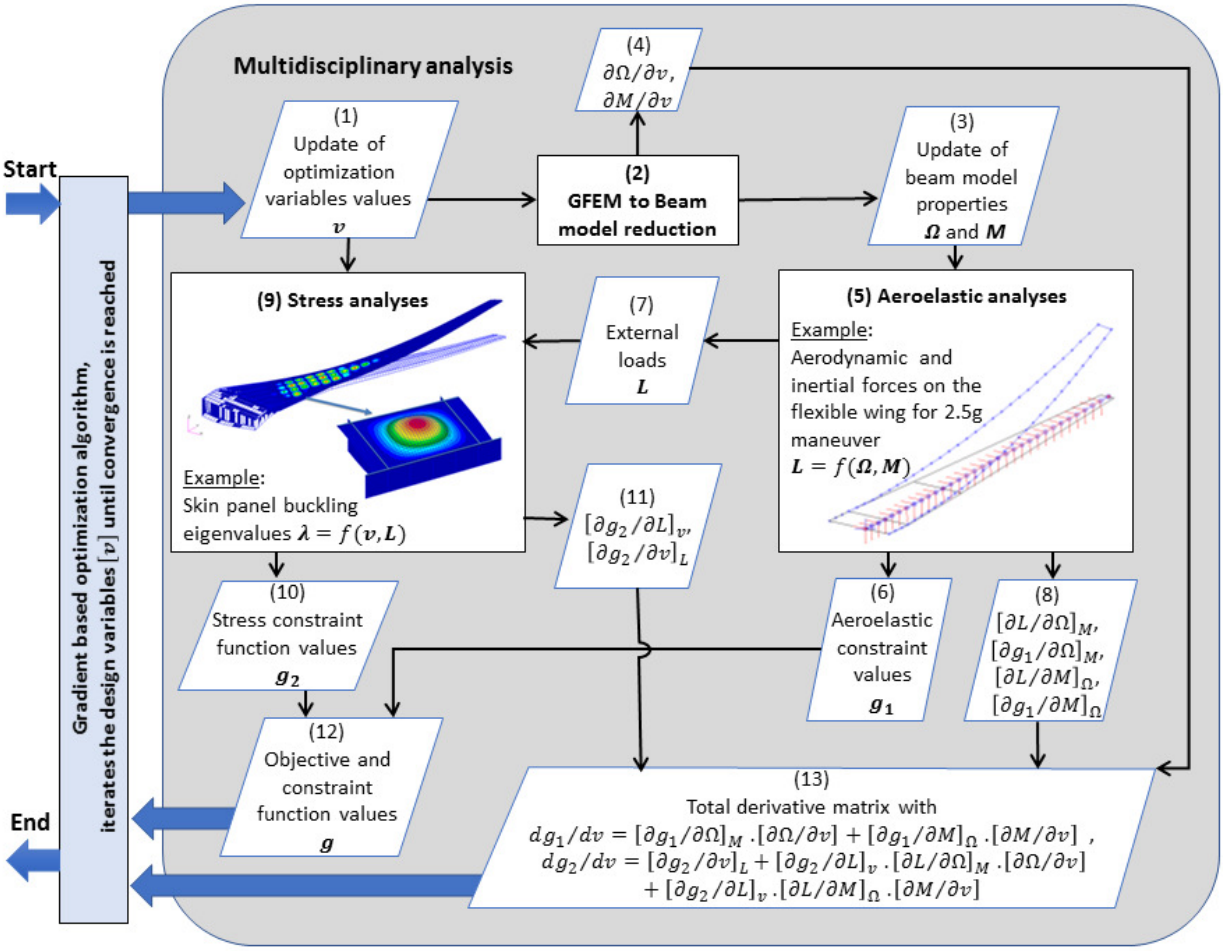

Fig. 1 Aeroelastic optimization with detailed stress constraints

example, the beam reduction yields the effective second moment of area I_1 for each beam element along the wing span and also its sensitivities to the GFEM optimization variables. Importantly, the reduction considered here does not make any presumption on the relations between the GFEM variables and beam properties. All beam properties, including the second moment of area I_1, are calculated from the GFEM static deflections due to tip loads as detailed in the next section. Aeroelastic analyses are then performed using the beam model (5), generating aeroelastic constraint values $\boldsymbol{g}_1$ (6), external loads $\boldsymbol{L}$ (7) and associated gradients with respect to the beam model properties (8). The external loads are applied to the GFEM model for stress analysis (9), which outputs the stress constraint values $\boldsymbol{g}_2$ (10) and their gradients with respect to the optimization variables $\partial g_2/\partial v$, and with respect to the applied loads $\partial g_2/\partial L$ (11). To complete the multidisciplinary analysis, the aggregated constraint function vector $\boldsymbol{g} = [g_1, g_2]$ (12) and total derivatives matrix $\partial g/\partial v$ (13), calculated by chain-ruling of the different analysis gradients, are returned to the optimization algorithm. The optimization objective function evaluation is not explicitly shown in Fig. 1, since it could be calculated at different stages of the multidisciplinary analysis process depending on the objective that is chosen. Typical objectives, such as

the wing weight or the cruise drag could be calculated in steps (9) or (5) respectively. In practice, to reduce the number of GFEM analyses to a minimum, only the most critical load cases should be selected for stress analysis in step (9), with all other stress constraints being considered inactive.

This approach differs from existing MDO implementations, which do not include the beam reduction (2) and associated data blocks (3), (4) and (8). In existing implementations, the GFEM is used for all analyses, so that steps (5) and (9) are effectively merged into a single multi-disciplinary analysis block. Moreover, as far as the authors are aware, whilst chain-ruling is a well-known method for calculating the total derivatives of system responses in a MDO context ([19]), the use of a chain rule to link GFEM and beam model partial derivatives for wing aeroelastic design purposes has not yet been explored in the literature. Clearly, integration of the beam reduction into the multidisciplinary analysis would allow for far more efficient aeroelastic computations, particularly as the number of aeroelastic analyses increases or as the number of GFEM degrees of freedom increases.

III. Stiffness reduction method

The wing GFEM to beam stiffness reduction process is performed in three successive steps: 1) the beam reference axis and beam element nodes are defined in the GFEM; 2) the beam element flexibility matrices are determined numerically from the deflection behavior of the GFEM due to a small number of static load cases; 3) a set of 13 physical isotropic beam stiffness parameters is calculated for each predefined element. The first two steps of this process can be performed using the blade property extraction (BPE) code described by Malcolm and Laird in reference [17]. It is the third step, which provides a reduced number of independent physical parameters and allows us to define an intermediate set of variables for gradient based optimization, that is developed in this paper. Note that linear structural analysis assumptions are made here, corresponding to small wing deflections and rotations, which is appropriate for a fast reduction method for design optimization purposes.

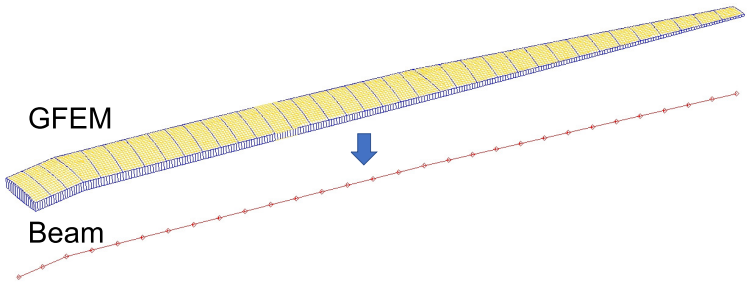

Fig. 2 Beam reduction concept

For a half-wing GFEM, as shown in figure 2, the beam reference axis corresponds to the line joining all beam element nodes from the root to the tip of the wing. The definition of the beam reference axis is trivial in that there is no specific requirement on its location, although it should be continuous and approximately aligned with the wing structure.

In particular, the reference axis may be straight over the whole wing, or have kinks where changes in wing dihedral or sweep occur. For each straight reference axis section, a xyz-local coordinate system (LCS) is defined as shown in figure 3, with the x-axis pointing from the beam node at the root of the section to that at the tip.

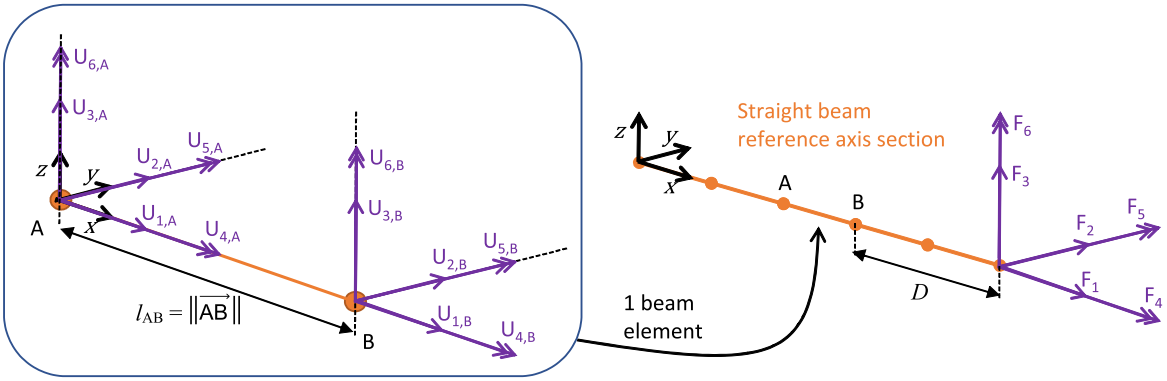

Fig. 3 Sign convention for nodal deflections (left) and for the applied forces/moments (right)

To determine the beam element flexibility matrices, a set of linear static GFEM analyses is performed for each straight reference axis section. First, existing boundary conditions on the GFEM are removed and replaced with a fixed boundary constraint at the wing root. The beam reference nodes are included in the GFEM and constrained to nearby shell elements, so that the beam nodes deflect and rotate with the surrounding structure. Then, 6 orthogonal forces and moments $\boldsymbol{F}$ are applied successively in the LCS directions at the tip of the current reference axis section, and the 6 orthogonal LCS displacements and rotations $\boldsymbol{U}$ of the current section beam nodes are output (see figure 3). The vector $\boldsymbol{U}$ is post-processed to extract the relative displacements and rotations vector $\boldsymbol{\Delta U}$ of each element's outboard node (B) with respect to the inboard node (A), such that

$$\boldsymbol{\Delta U_i} = \begin{cases} U_{i,B} - U_{i,A} & for \quad i = 1,4,5,6 \\ U_{i,B} - l_{AB}\, U_{6,A} - U_{i,A} & for \quad i = 2 \\ U_{i,B} + l_{AB}\, U_{5,A} - U_{i,A} & for \quad i = 3 \end{cases} \tag{1}$$

where degrees of freedom $i = 1,2,3$ and $i = 4,5,6$ correspond to the displacements and rotations in/about the LCS x, y and z directions respectively, and l_{AB} is the length of the beam element along the reference axis. Note that the contributions of the element rigid body rotations on the relative z- and y- displacements are removed using small rotation angle assumptions, with $\tan(U_{6,A}) \approx U_{6,A}$ and $\tan(U_{5,A}) \approx U_{5,A}$. Normalizing these relative displacements and rotations with respect to the force/moment vector $\boldsymbol{F}$, results in 36 equations defining each element of the 6x6 flexibility matrix $[C]$ as

$$[C]_{ij} = \begin{cases} \Delta U_i/F_j & for \quad i = \text{1-6 and } j = 1,4,5,6 \\ \Delta U_i/F_j - C_{i6}\, D & for \quad i = \text{1-6 and } j = 2 \\ \Delta U_i/F_j + C_{i5}\, D & for \quad i = \text{1-6 and } j = 3 \end{cases} \tag{2}$$

where D is the distance between the element node B and the node where the static shear forces F_2 and F_3 are applied. The inverse of matrix $[C]$ gives the corresponding stiffness matrix $[K]$ of the equivalent beam. In the following, the $[C]$ terms may be referred to both as the flexibility matrix terms and as the deflections and rotations corresponding to applied unit forces and moments.

This flexibility matrix calculation has some limitations, as already noted in reference [20] with respect to the BPE approach. The first limitation is associated with the assumption that the applied static tip forces and root boundary constraints result in strain fields representative of realistic wing load cases, where local load introduction effects are minimized. Spurious stiffness variations may occur if this assumption is not verified, as shown in the example in section A below. Another difficulty may arise when selecting GFEM element nodes to constrain the beam reference nodes. It may be preferable, for example, to define beam nodes in line with the rib planes in the GFEM to minimize the effect of local skin panel deflections on the output beam node deflections. Local deflections may also result in flexibility matrices that are not exactly symmetric, particularly for highly asymmetric and anisotropic cross sections. Finally, the beam element flexibility may alter significantly as the element length is varied. Despite these limitations, the BPE method has been shown to correlate well with experimental data and analytical beam models [21–25].

Subsequent steps, described in sections A to E, are used to derive 13 physical isotropic beam element stiffness parameters from the flexibility matrix $[C]$. These parameters, which result in an equivalent flexibility behavior to the GFEM, can be aggregated in a stiffness properties vector $\mathbf{\Omega} = [SC_{Ay}, SC_{Az}, SC_{By}, SC_{Bz}, \bar{\bar{J}}, \bar{\bar{I}}_1, \bar{\bar{I}}_2, \bar{\bar{I}}_{12}, \bar{\bar{N}}_y, \bar{\bar{N}}_z, \bar{\bar{A}}, \bar{\bar{k}}_y, \bar{\bar{k}}_z]^T$ for each beam element. These quantities are typically required to define the properties of an isotropic FEM model beam element. The first 4 terms of $\mathbf{\Omega}$ correspond to shear center offsets from the beam reference axis at nodes A and B (see section A). These offsets define the element elastic axis and drive the bend-twist coupling behavior of the beam. It should be noted, that the linear dependency of the shear center on the location along the beam reference axis for beams with anisotropic material properties is well known [10, 26, 27]. The remaining parameters are defined with respect to the elastic axis: the bending and torsion stiffness parameters ($\bar{\bar{J}}$ to $\bar{\bar{I}}_{12}$, section B), the location of the section centroid ($\bar{\bar{N}}_y$, $\bar{\bar{N}}_z$, section C), the section area ($\bar{\bar{A}}$, section D) and the shear coefficients ($\bar{\bar{k}}_y$, $\bar{\bar{k}}_z$, section E). It should be noted that no parameters are defined to quantify the beam warping behavior or shear relief due to box section taper. These effects are implicitly included in the calculation of the torsion constant $\bar{\bar{J}}$ and of the shear coefficients $\bar{\bar{k}}_y$, $\bar{\bar{k}}_z$. Finally, non-dimensional bend-twist coupling parameters as defined by Weisshaar [28] and of the form $\Psi = K/\sqrt{GJ.EI}$

are evaluated. These non-dimensional parameters can be used to classify a wing structure as being highly coupled ($|\Psi|$ close to 1) or lightly coupled ($|\Psi|$ close to 0). For this purpose, we relate Ψ to the previously listed beam element stiffness parameters in section F.

A. Beam element elastic axis and shear center offsets

Bend-twist coupling (corresponding to non-zero C_{45} and/or C_{46} values in equation (2)) is modeled here as a rotation of the beam element elastic axis (defined as the locus of shear centers) with respect to the x-direction of the LCS, as shown in figure 4. By definition, bending and torsion deflections are decoupled along the elastic axis, so that the unknown rotation angles γ_y and γ_z of the elastic axis with respect to the x-direction may be determined by setting the bend-twist coupling terms $\bar{C}_{45}$ and $\bar{C}_{46}$ of the elastic axis flexibility matrix $[\bar{C}]$ to zero.

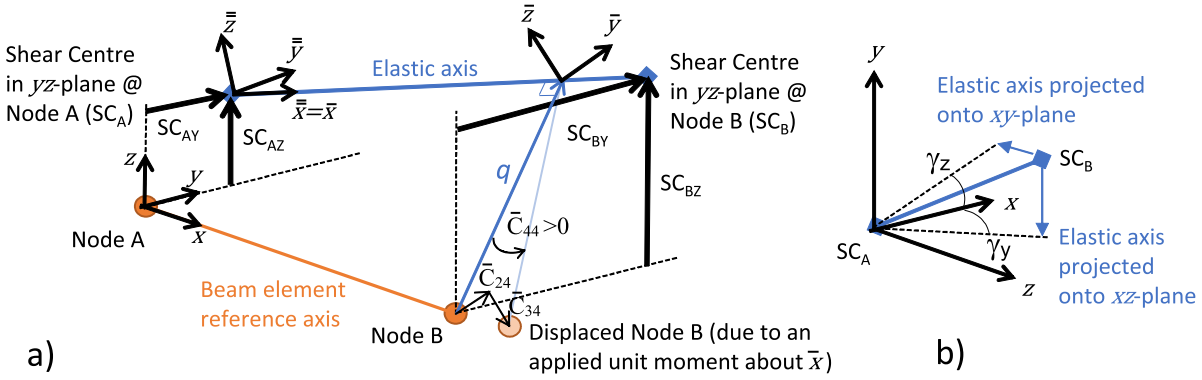

Fig. 4 Beam element elastic axis and shear center offset definitions (a), elastic axis rotation angles (b)

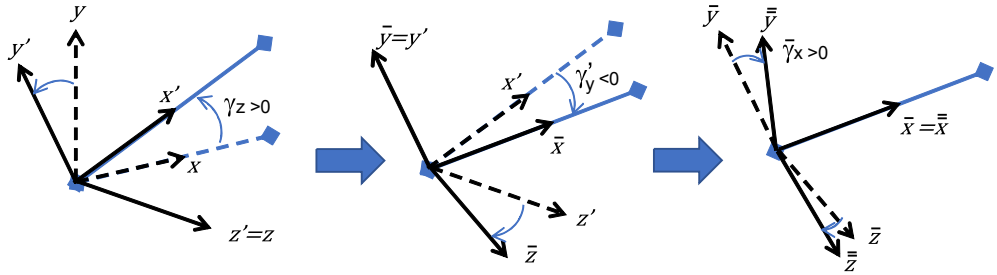

Fig. 5 Definition of the rotation angles γ_z, γ_y' and $\bar{\gamma}_x$, for successive rotations about the z, y' and $\bar{x}$ directions

This approach is implemented by defining the rotated flexibility matrix $[\bar{C}]$ as

$$[\bar{C}] = \begin{bmatrix} T & 0 \\ 0 & T \end{bmatrix} . [C] . \begin{bmatrix} T & 0 \\ 0 & T \end{bmatrix}^{-1} \quad \text{with } T = \begin{bmatrix} cy & 0 & -sy \\ 0 & 1 & 0 \\ sy & 0 & cy \end{bmatrix} \cdot \begin{bmatrix} cz & sz & 0 \\ -sz & cz & 0 \\ 0 & 0 & 1 \end{bmatrix}$$

$$\text{and} \qquad cy = \cos(\gamma'_y),\ sy = \sin(\gamma'_y),\ cz = \cos(\gamma_z),\ sz = \sin(\gamma_z),$$

$$\gamma_y = \tan^{-1}(sy/(cycz)). \tag{3}$$

where $[T]$ is the rotation matrix from the LCS to the elastic axis coordinate system, and the Euler rotation angles γ_z and γ'_y about the z and y'-axes (see figure 5) are calculated by solving the nonlinear system of equations

$$\begin{aligned} \bar{C}_{45} = 0 = &-C_{65}\, cz\, sy + C_{64}\, sy\, sz + C_{45}\, cy\, cz^2 - C_{54}\, cy\, sz^2 - C_{44}\, cy\, cz\, sz \\ &+C_{55}\, cy\, cz\, sz\,, \\ \bar{C}_{46} = 0 = &\, C_{46}\, cy^2\, cz + C_{56}\, cy^2\, sz - C_{64}\, cz\, sy^2 - C_{65}\, sy^2\, sz + C_{44}\, cy\, cz^2\, sy \\ &-C_{66}\, cy\, sy + C_{55}\, cy\, sy\, sz^2 + C_{45}\, cy\, cz\, sy\, sz + C_{54}\, cy\, cz\, sy\, sz. \end{aligned} \tag{4}$$

An iterative numerical solver (for example the trust-region algorithm as implemented in "fsolve" in Matlab [29]) may be used to find approximate solutions to equations (4), and this approach was found to yield accurate results for the examples in section V.

Once $[\bar{C}]$ has been determined, the equivalent shear center offsets in the LCS y- and z-directions at nodes A and B may be calculated. The normalized deflections $\bar{C}_{34}$ and $\bar{C}_{24}$ associated with a rotation $\bar{C}_{44}$ at node B (see Fig. 4) are used to determine the shortest vector $\boldsymbol{q}$ from node B to the element elastic axis in the LCS as

$$\boldsymbol{q} = T^{-1}\ [0,\ -\bar{C}_{34}/\tan(\bar{C}_{44}),\ \bar{C}_{24}/\tan(\bar{C}_{44})]^T, \tag{5}$$

where small angle assumptions are used to find $\tan(\bar{C}_{44}) \approx \bar{C}_{24}/\bar{q}_3$ and $\tan(\bar{C}_{44}) \approx -\bar{C}_{34}/\bar{q}_2$, with $\bar{\boldsymbol{q}} = T\boldsymbol{q}$. By projecting the end-point of $\boldsymbol{q}$ along the elastic axis onto the LCS yz-plane passing through node B, the local shear center offset vector at node B is determined as

$$\boldsymbol{SC_B} = [0,\ SC_{By},\ SC_{Bz}]^T = \boldsymbol{q} - q_1\, T^{-1}.[1,0,0]^T / \left(T^{-1}\right)_{11} \tag{6}$$

and the shear center offset vector at node A is deduced from SC_{By}, SC_{Bz} and the extrinsic rotation angles γ_y and γ_z as

$$\boldsymbol{SC_A} = [0,\, SC_{Ay},\, SC_{Az}]^T = \boldsymbol{SC_B} - l\,[0,\, \tan(\gamma_z),\, -\tan(\gamma_y)]^T . \tag{7}$$

In the most general case $\boldsymbol{SC_B} \neq \boldsymbol{SC_A}$; however, $\boldsymbol{SC_B} = \boldsymbol{SC_A}$ in the case where no bend-twist coupling exists ($\gamma_y = 0$ and $\gamma_z = 0$), but shear loads applied at node B result in torsion about the beam element reference axis (simple homogeneous prismatic beam case). Also, $\boldsymbol{SC_B} = -\boldsymbol{SC_A}$ for pure bend-twist coupling, due to anisotropic material properties and/or variable beam section geometry where the average beam section shear center offset of the element is zero.

B. Beam element bending and torsion stiffness along the elastic axis

The torsion constant $\bar{\bar{J}}$ is determined from the torsional flexibility $\bar{C}_{44}$ along the elastic axis, the effective length of the element along the elastic axis $L_{AB} = l_{AB}/(\cos(\gamma_y)\cos(\gamma_z))$ and the known material shear modulus G as

$$\bar{C}_{44} = L_{AB}/(G\bar{\bar{J}}) \Rightarrow \bar{\bar{J}} = l_{AB}\,\left[G\bar{C}_{44}\cos(\gamma_z)\cos(\gamma_y)\right]^{-1} . \tag{8}$$

We then define the element second moments of area $\bar{\bar{I}}_1$, $\bar{\bar{I}}_2$ and $\bar{\bar{I}}_{12}$ with respect to a rotated local coordinate system RLCS, where the $\bar{\bar{x}}$-direction is aligned with the elastic axis and the $\bar{\bar{z}}$ and $\bar{\bar{y}}$ direction unit vectors are defined in the LCS by an arbitrary input element orientation vector $\boldsymbol{p} = [0, 1, 0]^T$ as

$$\bar{\bar{z}} = \bar{\bar{x}} \times \boldsymbol{p} = [T_{11}, T_{21}, T_{31}]^T \times \boldsymbol{p}\,, \qquad \bar{\bar{y}} = \bar{\bar{z}} \times \bar{\bar{x}}\,. \tag{9}$$

In general, $\bar{\bar{y}} \neq \bar{y}$ so an additional rotation of the flexibility matrix $[\bar{C}]$ about the elastic axis ($\bar{x}$-direction) is required to determine the second moments of area, resulting in the flexibility matrix $[\bar{\bar{C}}]$ being found as

$$[\bar{\bar{C}}] = \begin{bmatrix} T_1 & 0 \\ 0 & T_1 \end{bmatrix} . [\bar{C}] . \begin{bmatrix} T_1 & 0 \\ 0 & T_1 \end{bmatrix}^{-1} \text{ with } T_1 = \begin{bmatrix} 1 & 0 & 0 \\ 0 & cx & -sx \\ 0 & sx & cx \end{bmatrix}$$
$$\text{and} \qquad cx = \cos(\bar{\gamma}_x),\ sx = \sin(\bar{\gamma}_x),\ \bar{\gamma}_x = \tan^{-1}(-\bar{p}_3/\bar{p}_2),\ \bar{\boldsymbol{p}} = T\boldsymbol{p}. \tag{10}$$

Using beam theory, a system of linear equations in $\bar{\bar{I}}_1$, $\bar{\bar{I}}_2$ and $\bar{\bar{I}}_{12}$ can then be derived as

$$\begin{bmatrix} \bar{\bar{F}}_5 \\ \bar{\bar{F}}_6 \end{bmatrix} = \frac{E}{L_{AB}} \cdot \begin{bmatrix} \bar{\bar{I}}_2 & \bar{\bar{I}}_{12} \\ \bar{\bar{I}}_{12} & \bar{\bar{I}}_1 \end{bmatrix} \cdot \begin{bmatrix} \Delta\bar{\bar{U}}_5 \\ \Delta\bar{\bar{U}}_6 \end{bmatrix} \Rightarrow \begin{bmatrix} 1 \\ 0 \\ 0 \\ 1 \end{bmatrix} = \frac{E}{L_{AB}} \cdot \begin{bmatrix} 0 & \bar{\bar{C}}_{65} & \bar{\bar{C}}_{55} \\ \bar{\bar{C}}_{65} & \bar{\bar{C}}_{55} & 0 \\ 0 & \bar{\bar{C}}_{66} & \bar{\bar{C}}_{56} \\ \bar{\bar{C}}_{66} & \bar{\bar{C}}_{56} & 0 \end{bmatrix} \cdot \begin{bmatrix} \bar{\bar{I}}_1 \\ \bar{\bar{I}}_{12} \\ \bar{\bar{I}}_2 \end{bmatrix} . \tag{11}$$

where E is the known material Young's modulus. The overdetermined system of equations on the right-hand side of equation (11) includes the special cases where $\bar{\bar{F}}_5$ and $\bar{\bar{F}}_6$ take the zero value. Although setting either $\bar{\bar{F}}_5 = 0$ or $\bar{\bar{F}}_6 = 0$ would be sufficient to solve for the stiffness terms, it is preferable to retain both special cases, since the BPE method is known to potentially result in slightly asymmetric flexibility matrices ($\bar{\bar{C}}_{65} \neq \bar{\bar{C}}_{56}$). In this case, the Moore-Penrose pseudo-inverse can be used to find the "best fit" or least squares solution for $\bar{\bar{I}}_1$, $\bar{\bar{I}}_2$ and $\bar{\bar{I}}_{12}$.

C. Beam element average centroid location with respect to the elastic axis

The beam centroid location with respect to the elastic axis may be determined by calculating the orientation of the beam section principal axes with respect to the RLCS $\bar{\bar{y}}$ and $\bar{\bar{z}}$-directions, and then finding the neutral plane intersection due to moments about the principal axes. We define $[\bar{\bar{C}}_p]$ as the beam flexibility matrix in the beam principal axes system where $\bar{\bar{C}}_{p,56} = \bar{\bar{C}}_{p,65} = 0$, so that

$$[\bar{\bar{C}}_p] = \begin{bmatrix} T_p & 0 \\ 0 & T_p \end{bmatrix} . [\bar{\bar{C}}] . \begin{bmatrix} T_p & 0 \\ 0 & T_p \end{bmatrix}^{-1} \quad \text{with } T_p = \begin{bmatrix} 1 & 0 & 0 \\ 0 & cx_p & sx_p \\ 0 & -sx_p & cx_p \end{bmatrix}$$

$$\text{and} \qquad cx_p = \cos(\bar{\gamma}_{xp}),\ sx_p = \sin(\bar{\gamma}_{xp}),\ \bar{\gamma}_{xp} = 0.5\tan^{-1}(-2\bar{\bar{C}}_{56}/(\bar{\bar{C}}_{66} - \bar{\bar{C}}_{55})). \tag{12}$$

Beam kinematics are used to derive the centroid offsets $\bar{\bar{N}}_{yp}, \bar{\bar{N}}_{zp}$ from the elastic axis in the principal axis system as

$$\begin{aligned} \bar{\bar{N}}_{zp} &= (\bar{\bar{C}}_{p,15} - r_1\cos(\bar{\bar{C}}_{p,55}) - r_3\sin(\bar{\bar{C}}_{p,55}) + r_1)\tan(\pi/2 + \bar{\bar{C}}_{p,55}) \\ \bar{\bar{N}}_{yp} &= -(\bar{\bar{C}}_{p,16} - r_1\cos(\bar{\bar{C}}_{p,66}) + r_2\sin(\bar{\bar{C}}_{p,66}) + r_1)\tan(\pi/2 + \bar{\bar{C}}_{p,66}) \\ &\text{with} \qquad \boldsymbol{r} = -T_p \,.\, T_1 \,.\, T \,.\, \boldsymbol{SC_B} \,. \end{aligned} \tag{13}$$

The centroid offsets $\bar{\bar{N}}_y, \bar{\bar{N}}_z$ from the elastic axis in the RLCS system may then be determined from

$$[0, \bar{\bar{N}}_y, \bar{\bar{N}}_z]^T = T_p^{-1}\,[0, \bar{\bar{N}}_{yp}, \bar{\bar{N}}_{zp}]^T \,. \tag{14}$$

D. Beam element equivalent area along the elastic axis

The section area $\bar{\bar{A}}$ is a function of the element extension in the RLCS $\bar{\bar{x}}$-direction due to a tensile force applied through the section centroid. This extension is calculated by first determining the deflections at node B due only to the moment about the centroid generated by a unit tensile force being applied at node B, and then subtracting these deflections from $\bar{\bar{C}}_{11}$, such that

$$\begin{aligned} \bar{\bar{A}} &= L_{AB}/E\,(\bar{\bar{C}}_{11} - \Delta\bar{\bar{U}}_1)^{-1} \\ \text{with} \quad \boldsymbol{\Delta\bar{\bar{U}}} = [\bar{\bar{C}}]\,.\,\bar{\bar{\boldsymbol{F}}}\,, &\quad \bar{\bar{\boldsymbol{F}}}_{\mathbf{1-3}} = [0,0,0]^T\,, \quad \bar{\bar{\boldsymbol{F}}}_{\mathbf{4-6}} = \boldsymbol{w} \times [1,0,0]^T\,, \\ \text{and} \quad \boldsymbol{w} &= -T_1\,.\,T\,.\,\boldsymbol{SC_B} - [0, \bar{\bar{N}}_y, \bar{\bar{N}}_z]^T\,. \end{aligned} \tag{15}$$

E. Beam element shear coefficients along the elastic axis

Finally, the Timoshenko beam theory shear coefficients $\bar{\bar{k}}_y, \bar{\bar{k}}_z$ in the RLCS $\bar{\bar{y}}$ and $\bar{\bar{z}}$-directions are determined by subtracting the deflection $\bar{\bar{\delta}}_y, \bar{\bar{\delta}}_z$ due to bending strains from the total shear deflections at the elastic axis, so that

$$\begin{aligned} \bar{\bar{k}}_y &= L_{AB}/(AG)\,.\,(\bar{\bar{C}}_{22} - \Delta\bar{\bar{U}}_{\alpha,2} - \Delta\bar{\bar{U}}_{\beta,2} - \bar{\bar{\delta}}_y)^{-1} \\ \text{with} \quad \boldsymbol{\Delta\bar{\bar{U}}_\alpha} = [\bar{\bar{C}}]\,.\,\bar{\bar{\boldsymbol{F}}}\,, &\quad \bar{\bar{\boldsymbol{F}}}_{\mathbf{1-3}} = [0,0,0]^T\,, \quad \bar{\bar{\boldsymbol{F}}}_{\mathbf{4-6}} = \boldsymbol{u} \times [0,1,0]^T\,, \\ \boldsymbol{\Delta\bar{\bar{U}}_\beta} &= \begin{bmatrix} cz & -sz & 0 \\ sz & cz & 0 \\ 0 & 0 & 1 \end{bmatrix} \cdot \begin{bmatrix} cy & 0 & sy \\ 0 & 1 & 0 \\ -sy & 0 & cy \end{bmatrix} . \boldsymbol{u} - \boldsymbol{u} \\ \bar{\bar{\delta}}_y &= 2L_{AB}/3\,.\,(\bar{\bar{C}}_{62} - \Delta\bar{\bar{U}}_{\alpha,6}) \\ \text{and} \quad cy = \cos(\bar{\bar{C}}_{52} - \Delta\bar{\bar{U}}_{\alpha,5}),&\ sy = \sin(\bar{\bar{C}}_{52} - \Delta\bar{\bar{U}}_{\alpha,5}), \\ cz = \cos(\bar{\bar{C}}_{62} - \Delta\bar{\bar{U}}_{\alpha,6}),&\ sz = \sin(\bar{\bar{C}}_{62} - \Delta\bar{\bar{U}}_{\alpha,6}), \\ \boldsymbol{u} &= -T_1\,.\,T\,.\,\boldsymbol{SC_B} \end{aligned} \tag{16}$$

and

$$\bar{\bar{k}}_z = L_{AB}/(AG)\,.\,(\bar{\bar{C}}_{33} - \Delta\bar{\bar{U}}_{\alpha,3} - \Delta\bar{\bar{U}}_{\beta,3} - \bar{\bar{\delta}}_z)^{-1}$$

$$\text{with} \quad \boldsymbol{\Delta\bar{\bar{U}}_{\alpha}} = [\bar{\bar{C}}]\,.\,\boldsymbol{\bar{\bar{F}}}\,, \quad \boldsymbol{\bar{\bar{F}}_{1-3}} = [0,0,0]^T\,, \quad \boldsymbol{\bar{\bar{F}}_{4-6}} = \boldsymbol{u} \times [0,0,1]^T\,,$$

$$\boldsymbol{\Delta\bar{\bar{U}}_{\beta}} = \begin{bmatrix} cz & -sz & 0 \\ sz & cz & 0 \\ 0 & 0 & 1 \end{bmatrix} \cdot \begin{bmatrix} cy & 0 & sy \\ 0 & 1 & 0 \\ -sy & 0 & cy \end{bmatrix} . \boldsymbol{u} - \boldsymbol{u}$$

$$\bar{\bar{\delta}}_y = -2L_{AB}/3\,.\,(\bar{\bar{C}}_{53} - \Delta\bar{\bar{U}}_{\alpha,5}) \tag{17}$$

$$\text{and} \quad cy = \cos(\bar{\bar{C}}_{53} - \Delta\bar{\bar{U}}_{\alpha,5}),\ sy = \sin(\bar{\bar{C}}_{53} - \Delta\bar{\bar{U}}_{\alpha,5}),$$

$$cz = \cos(\bar{\bar{C}}_{63} - \Delta\bar{\bar{U}}_{\alpha,6}),\ sz = \sin(\bar{\bar{C}}_{63} - \Delta\bar{\bar{U}}_{\alpha,6}),$$

$$\boldsymbol{u} = -T_1\,.\,T\,.\,\boldsymbol{SC_B}.$$

This completes the calculation of $\mathbf{\Omega}$ for an element. We now consider how the terms of $\mathbf{\Omega}$ relate to the non-dimensional bend-twist coupling parameter Ψ.

F. Evaluation of non-dimensional stiffness coupling parameters

The following relations apply for isotropic and composite wings, assuming that extension-bending coupling of the wing can be neglected. The internal beam bending moments F_5, F_6 and torque F_4 are related to the beam curvatures δ_z'', δ_y'' and twist rate α_x' along the local beam reference axis x as

$$\begin{bmatrix} F_4 \\ F_5 \\ F_6 \end{bmatrix} = \begin{bmatrix} GJ & K_2 & K_1 \\ K_2 & EI_2 & EI_{12} \\ K_1 & EI_{12} & EI_1 \end{bmatrix} \begin{bmatrix} \alpha_x' \\ \delta_z'' \\ \delta_y'' \end{bmatrix}, \tag{18}$$

with the equivalent flexibility relation being

$$\begin{bmatrix} \alpha_x' \\ \delta_z'' \\ \delta_y'' \end{bmatrix} = Q^{-1} \begin{bmatrix} EI_1\,EI_2 - {EI_{12}}^2 & EI_{12}\,K_1 - EI_1\,K_2 & EI_{12}\,K_2 - EI_2\,K_1 \\ EI_{12}\,K_1 - EI_1\,K_2 & EI_1\,GJ(1-{\Psi_1}^2) & K_1\,K_2 - EI_{12}\,GJ \\ EI_{12}\,K_2 - EI_2\,K_1 & K_1\,K_2 - EI_{12}\,GJ & EI_2\,GJ(1-{\Psi_2}^2) \end{bmatrix} \begin{bmatrix} F_4 \\ F_5 \\ F_6 \end{bmatrix},$$

$$\text{with} \qquad Q = GJ\left(EI_1EI_2 - {EI_{12}}^2\right)\left(1 - \frac{{\Psi_1}^2 + {\Psi_2}^2 - 2\Psi_1\Psi_2 EI_{12}/(EI_1EI_2)^{1/2}}{1 - {EI_{12}}^2/(EI_1EI_2)}\right), \tag{19}$$

where the two non-dimensional bend-twist coupling parameters Ψ_{11} and Ψ_{22} are defined as

$$\Psi_1 = K_1/(GJ.EI_1)^{1/2} \qquad \text{and} \qquad \Psi_2 = K_2/(GJ.EI_2)^{1/2}. \tag{20}$$

It should be noted that the feasible domains of Ψ_1 and Ψ_2 are not independent, since strain energy considerations require not only $-1 < \Psi_1 < 1$ and $-1 < \Psi_2 < 1$, but also $Q > 0$ in equation (19), which corresponds to

$$1 > \frac{{\Psi_1}^2 + {\Psi_2}^2 - 2\Psi_1\Psi_2 EI_{12}/(EI_1EI_2)^{1/2}}{1 - (EI_{12})^2/(EI_1EI_2)} \geq 0,$$
$$\text{with } -1 < EI_{12}/(EI_1EI_2)^{1/2} < 1. \tag{21}$$

To evaluate Ψ_1 and Ψ_2 in equation (20), it is necessary to determine the stiffness matrix in equation (18), which can be related to the known beam element elastic axis stiffness matrix using the previously defined rotation matrices and rotation angles as

$$\begin{bmatrix} GJ & K_2 & K_1 \\ K_2 & EI_2 & EI_{12} \\ K_1 & EI_{12} & EI_1 \end{bmatrix} = \cos(\gamma_y)\cos(\gamma_z)\, T^{-1}\, T_1^{-1} \begin{bmatrix} G\bar{\bar{J}} & 0 & 0 \\ 0 & E\bar{\bar{I}}_2 & E\bar{\bar{I}}_{12} \\ 0 & E\bar{\bar{I}}_{12} & E\bar{\bar{I}}_1 \end{bmatrix} T_1\, T\,. \tag{22}$$

In this equation, the factor $\cos(\gamma_y)\cos(\gamma_z)$ is included to account for the "stretching" of the elastic axis with respect to the beam element length for non-zero γ_y or γ_z rotation angles. The non-dimensional stiffness coupling parameters can therefore be determined within the stiffness reduction process.

IV. Mass reduction method

"Lumped" mass and inertia properties are calculated at the beam nodes to approximate the distributed mass properties of the GFEM along the wing span. In a first step, the GFEM model is split into element groups associated with each beam node, defining the integration volumes for the lumped mass and inertia properties. For each group of elements, the equivalent mass m_s, center of gravity (CG) location and inertia with respect to the beam node in the global coordinate

system are then determined as

$$
\begin{gathered}
m_s = \sum_{i=1}^{n} m_i \,, \\
X_{CG} = \sum_{i=1}^{n} m_i X_i / m_s \,, \qquad Y_{CG} = \sum_{i=1}^{n} m_i Y_i / m_s \,, \qquad Z_{CG} = \sum_{i=1}^{n} m_i Z_i / m_s \,, \\
I_{XX} = \sum_{i=1}^{n} m_i \left(Y_i^2 + Z_i^2\right) \,, \quad I_{YY} = \sum_{i=1}^{n} m_i \left(X_i^2 + Z_i^2\right) \,, \quad I_{ZZ} = \sum_{i=1}^{n} m_i \left(Y_i^2 + X_i^2\right) \,, \\
I_{XY} = \sum_{i=1}^{n} m_i X_i Y_i \,, \qquad I_{XZ} = \sum_{i=1}^{n} m_i X_i Z_i \,, \qquad I_{YZ} = \sum_{i=1}^{n} m_i Y_i Z_i \,,
\end{gathered}
\tag{23}
$$

where m_i, X_i, Y_i and Z_i are the mass of element i and the distance of its centroid from the beam node. The 6×6 symmetric mass matrix $[M]$ at the beam node may then be determined from

$$
[M] = \begin{bmatrix}
m_s & & & & & \\
0 & m_s & & \text{sym.} & & \\
0 & 0 & m_s & & & \\
0 & (-m_s Z_{CG}) & (m_s Y_{CG}) & I_{XX} & & \\
(m_s Z_{CG}) & 0 & (-m_s X_{CG}) & -I_{XY} & I_{YY} & \\
(-m_s Y_{CG}) & (m_s X_{CG}) & 0 & -I_{XZ} & -I_{YZ} & I_{ZZ}
\end{bmatrix}
\tag{24}
$$

Using MSC Nastran, this mass reduction is conveniently implemented by defining super-elements (SE) along the wing span and running the grid point weight generator. The mass matrix is subsequently used to automatically define discrete mass elements.

V. Reduction examples

A. Constant-section rectangular wing-box

A constant-section rectangular wing-box GFEM of 16.8m span, 1.68m chord and 1.0m height is used to illustrate the reduction method. In addition, the effects on the stiffness parameter variations associated with an increase in the front spar thickness, the use of unbalanced laminates in the skin, and the rotation of a rib are studied. The baseline wing-box configuration features 8mm thick quasi-isotropic composite spars, 2mm thick metallic ribs and 10mm thick skins with a high percentage of 0° fiber plies (44%) aligned with the global Y-direction. Reference equivalent beam properties calculated using the variational asymptotic beam sectional analysis (VABS) [10] are listed in Table 1. The FEM mesh is representative of a GFEM model used for internal loads calculations. The skins, spars and ribs are modeled using shell elements and the omega-stringers and spar caps are modeled using beam elements, with a mesh detail shown in Fig.6.

The beam reference axis, aligned with the global Y-direction, is defined at box mid-height and mid-chord, with the beam LCS y-direction pointing forward, in the global −X-direction. The baseline model section is symmetric with respect to the global XY- and ZY-planes. Beam nodes, defined at the intersections of the beam reference axis and the ribs, are splined to the wing skins using RBE3 elements, which correspond to multi-point constraint (MPC) relations in which the motion at the beam node is the least square uniformly weighted average of the motions at the skin nodes. A constant rib-pitch of 0.6m results in 28 beam elements.

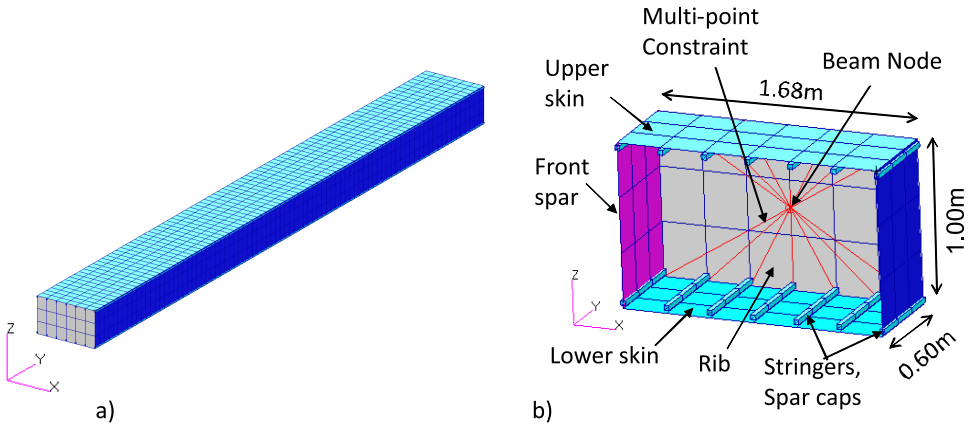

Fig. 6 Rectangular box GFEM model (a) and mesh detail for one rib-bay (b)

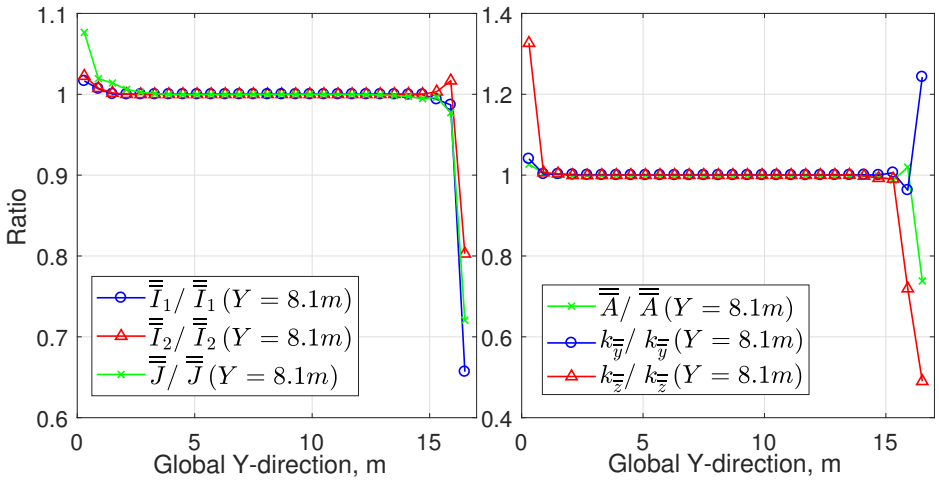

Fig. 7 Baseline model equivalent beam stiffness parameter variations with respect to the mid-span values, listed in Table 1

The baseline model equivalent beam stiffness properties for each beam element are calculated using the equations from sections A to E. The properties calculated at mid-span (Y=8.1m) are compared to the VABS reference properties in Table 1, where errors in $E\bar{\bar{I}}_1$, $E\bar{\bar{I}}_2$, $G\bar{\bar{J}}$ and $\bar{\bar{A}}$ are below 5%, whereas the shear coefficients $\bar{\bar{k}}_y$ and $\bar{\bar{k}}_z$ are significantly smaller than those predicted by VABS. It should be noted, that the VABS and GFEM models use different wingbox

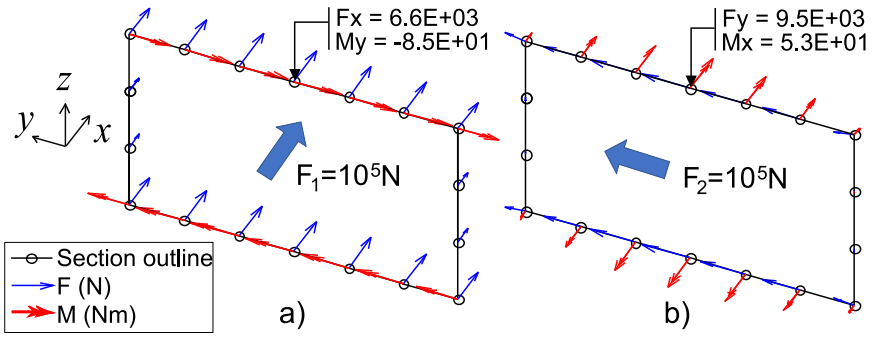

Fig. 8 Nodal force (F) and moment (M) distributions at the wing tip section corresponding to applied tip forces F_1 (a) and F_2 (b)

section modeling assumptions (e.g. different element mesh densities; different element types; different stringer and material idealizations), so that differences in the equivalent beam stiffness parameters are not unexpected. For example, the stringer cross-section shapes and stringer flange attachments are modeled accurately in VABS, but not in the GFEM, where equivalent stiffness 1D beam elements are used. The discrepancies between the reduced beam properties and VABS reference values are therefore not indicative of the accuracy of the reduction method. The accuracy of the beam reduction method is instead established by comparison of the GFEM and beam behaviors, as discussed later in this section.

The variations of the beam properties along the span are plotted in Fig. 7, where the symbols indicate the location of the center of each beam element. The shear center and neutral axis offsets, being zero along the span, are not plotted. An increase in stiffness at the wing root is linked to the fully fixed boundary condition, which constrains the warping of the section. Conversely, the beam stiffness is reduced at the wingtip, where the load introduction assumptions significantly affect the GFEM behavior. The MPC resolves the loads applied at the wingtip beam node into equivalent forces at the skin nodes, neglecting the stiffness variations and stringer offsets, so that the wingtip section deforms and the apparent beam axial and bending stiffness towards the wingtip is reduced. This behavior is a known limitation of the BPE method [21–23] and shows the importance of choosing appropriate boundary constraint and loading assumptions during the reduction. To minimize the effects of these assumptions, it may be preferable to determine a set of equivalent skin forces and moments at the wing root and tip, which minimize the section deformations without adding stiffness, for example using thin-walled beam theory or by extracting internal loads at an equivalent wing section several rib-bays removed from the wing-tip or root. The latter approach is demonstrated here, with a set of extracted nodal force and moment distributions plotted in Fig. 8, clearly showing that moments have to be applied at the skin nodes to account for the skin and stringers offsets from the FE shell mesh. The beam stiffness properties obtained by repeating the baseline GFEM reduction using the modified tip loads (MTL) and retaining a fully fixed wing root constraint are compared to the stiffness properties of the baseline reduction in Table 1. The beam stiffness variations at the wingtip with respect to

the mid-span position have been minimized using this approach.

a) $$[C]_0 = \begin{bmatrix} 0.0120 & 0 & 0 & 0 & 0 & 0 \\ 0 & 0.0996 & 0 & 0 & 0 & 0.0108 \\ 0 & 0 & 0.2106 & 0 & -0.0172 & 0 \\ 0 & 0 & 0 & 0.1447 & 0 & 0 \\ 0 & 0 & -0.0172 & 0 & 0.0574 & 0 \\ 0 & 0.0108 & 0 & 0 & 0 & 0.0358 \end{bmatrix} .10^{-8} ;$$

b) $$[C]_3 = \begin{bmatrix} 0.0112 & 0.0058 & 0 & 0 & 0 & 0.0028 \\ 0.0064 & 0.1236 & 0 & 0 & 0 & 0.0103 \\ 0 & 0 & 0.1727 & -0.0237 & -0.0178 & 0 \\ 0 & 0 & -0.0180 & 0.1544 & -0.0137 & 0 \\ 0 & 0 & -0.0166 & -0.0138 & 0.0563 & 0 \\ 0.0029 & 0.0101 & 0 & 0 & 0 & 0.0295 \end{bmatrix} .10^{-8} ;$$

Fig. 9 Flexibility matrix $[C]$ of the beam element at Y=8.1m in the baseline model (a) and model 3 (b) (in SI units)

Table 1 Comparison of the equivalent beam properties of the rectangular box models, where $E = 70.0E + 9$ and $G = 26.9E + 9$

	Mid-span element (Y=8.1m)				Wingtip element (Y=16.5m)		
Parameter	Baseline	Model 1	Model 2	Model 3	Baseline (RBE3)	Baseline (MTL)	Baseline (VABS)
SC_{Ay} (m)	0.00	0.20	0.21	0.22	0.00	0.00	0.00
SC_{Az} (m)	0.00	0.00	0.00	0.00	0.00	0.00	0.00
SC_{By} (m)	0.00	0.20	0.12	0.14	0.00	0.00	0.00
SC_{Bz} (m)	0.00	0.00	0.00	0.00	0.00	0.00	0.00
$G\bar{\bar{J}}$ $(N.m^2)$	4.14E+8	4.65E+8	3.85E+8	3.87E+8	2.99E+8	4.15E+8	4.06E+8
$E\bar{\bar{I}}_1$ $(N.m^2)$	1.67E+9	2.07E+9	2.05E+9	2.05E+9	1.10E+9	1.68E+9	1.65E+9
$E\bar{\bar{I}}_2$ $(N.m^2)$	1.04E+9	1.10E+9	1.11E+9	1.11E+9	8.39E+8	1.04E+9	1.04E+9
$E\bar{\bar{I}}_{12}$ $(N.m^2)$	0.00	0.00	0.00	0.00	0.00	0.00	0.00
$\bar{\bar{N}}_y$ (m)	0.00	-0.11	-0.08	-0.09	0.00	0.00	0.00
$\bar{\bar{N}}_z$ (m)	0.00	0.00	0.00	0.00	0.00	0.00	0.00
$\bar{\bar{A}}$ (m^2)	7.12E-2	8.01E-2	7.49E-2	7.45E-2	5.25E-2	7.12E-2	7.45E-2
$\bar{\bar{k}}_y$ (-)	0.33	0.29	0.25	0.25	0.41	0.32	1.42
$\bar{\bar{k}}_z$ (-)	0.15	0.19	0.18	0.19	0.08	0.15	0.26
Ψ_1 (-)	0.0	0.0	0.0	0.0	0.0	0.0	-
Ψ_2 (-)	0.0	0.0	0.148	0.147	0.0	0.0	-

Three modification are then incrementally performed on the baseline configuration to highlight their individual

effects: the front spar thickness is increased from 8mm to 20mm (model 1); the percentage of $+45/-45^\circ$ fibers in the upper and lower skin laminates is changed from 22%/22% to 40%/4% (model 2); the 2mm thick rib at y=8.4m is rotated by 20° around the global Z-axis (model 3). As an example, the changes in the flexibility matrix $[C]$ and of the associated stiffness parameters of a single beam element located at wing mid-span (Y=8.1m) are shown in Fig. 9 and in Table 1. The shear center offset variations along the wing span for models 1 to 3 are plotted in Fig. 10. As expected, the shear center offsets in the beam z-direction are zero for all configurations, due to the section symmetry with respect to the xy-plane. In model 1, the thickening of the front spar mainly increases the EI_1 bending stiffness and moves the elastic axis forward by 0.2m in the beam y-direction, with $SC_{By} = SC_{Ay}$. In model 2, the unbalanced skin laminates result in bend-twist coupling, corresponding to a rotation of the element elastic axes with respect to the beam reference axis (see Fig. 11), with $SC_{By} < SC_{Ay}$ and $\Psi_2 > 0$, along with a 17% reduction in the torsional stiffness along the elastic axis. The stiffness variations due to the rib rotation (model 3) are localized between Y=6.9m and Y=9.9m, with the shear centers moving forward for Y<8.4m, and moving aft for Y>8.4m.

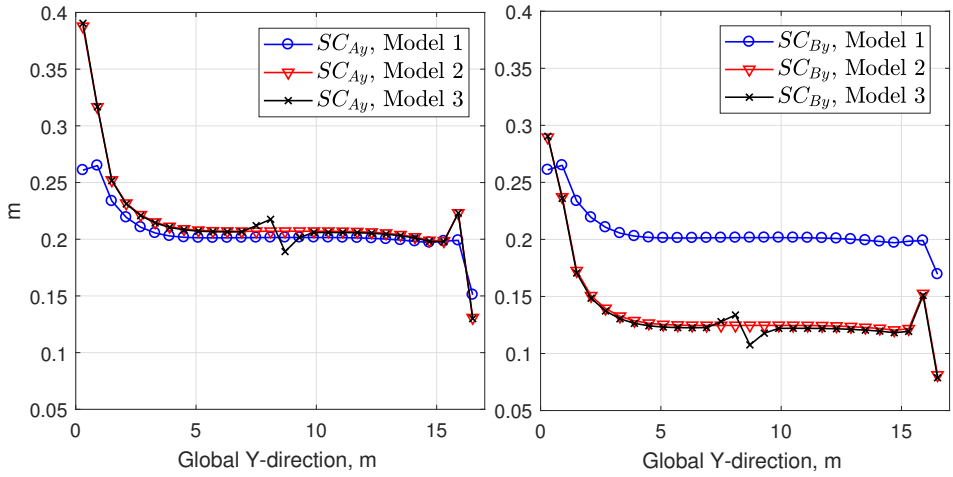

Fig. 10 Shear center offsets along the wing span for models 1 to 3

In order to verify the accuracy of the stiffness reductions, the GFEM and beam model wing tip displacements U and rotations R are compared for different applied tip loads, in the global XYZ-directions, in Table 2 and Fig. 12 and 13. The plots show the transition from the baseline to model 3 by firstly increasing the front spar thickness to model 1, then adjusting the +45° fiber ply percentage to model 2, and then the rib rotation to model 3. They show that the beam model deflection errors are smallest (<5%) for the baseline and model 1 configurations. The errors increase as the percentage of +45° fiber plies is increased, reaching maximum values for the model 2 configuration. Zoomed-in plot inserts show that the incremental tip deflections due to the rib rotation update in model 3 are orders of magnitude lower than the incremental deflections between the baseline and models 1 and 2. Hence, the rib rotation has no significant effect on the wing tip deflection errors summarized in Table 2. In this Table, most deflection errors are below 5%, with

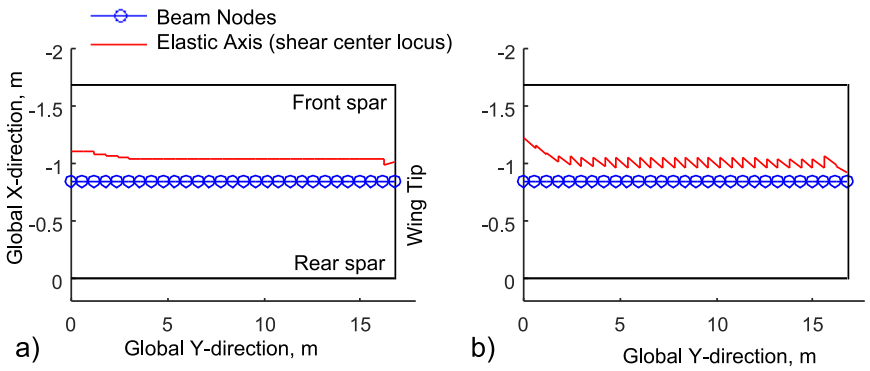

Fig. 11 Elastic axes for model 1 (a) and model 2 (b)

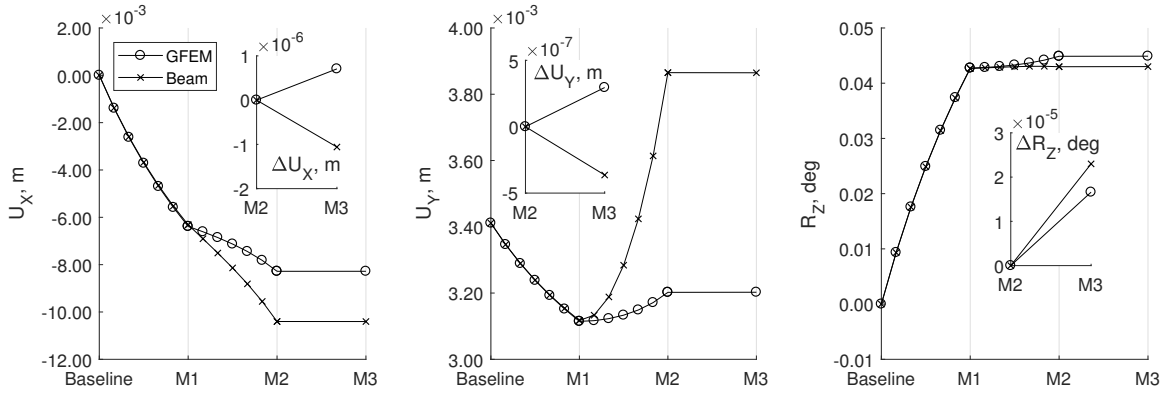

Fig. 12 GFEM and equivalent beam tip deflection variations due to incremental GFEM model updates, from the baseline to model 3 (M3), for an applied spanwise force F_Y=1.0E6N

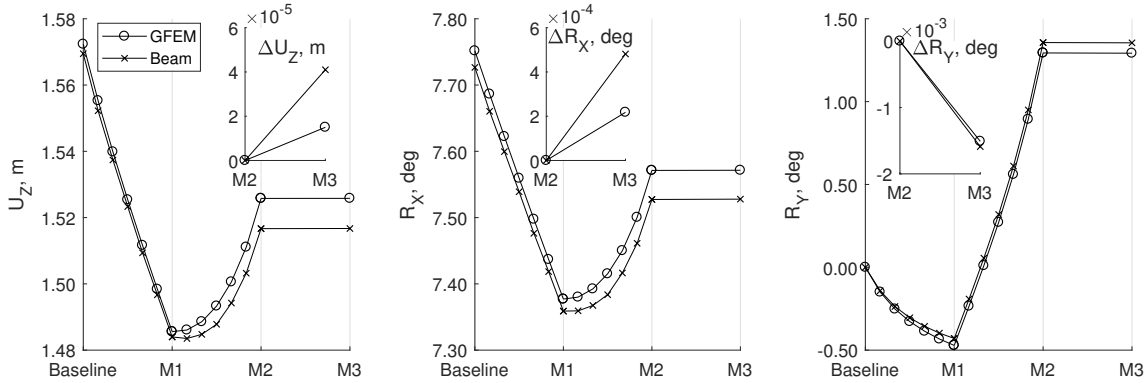

Fig. 13 GFEM and equivalent beam tip deflection variations due to incremental GFEM model updates, from the baseline to model 3 (M3), for an applied shear force F_Z=1.0E6N

the largest errors (20-25%) occurring for relatively small extension and shear-extension coupling deflections. Indeed, the box shear-extension stiffness coupling, which correspond to the flexibility matrix terms C_{12} and C_{13} and is due to the unbalanced skin laminates, cannot be accurately captured using this beam reduction method. As a result, the beam

Table 2 Comparison of the Model 3 GFEM and equivalent beam tip deflections due to applied tip loads in the global XYZ-directions

	F_X=1.0E6N			F_Y=1.0E6N			F_Z=1.0E6N		
	GFEM	Beam	Δ(%)	GFEM	Beam	Δ(%)	GFEM	Beam	Δ(%)
U_X (m)	8.11E-1	8.06E-1	-0.6	-8.28E-3	-1.04E-2	25.6	0.00E+0	0.00E+0	-
U_Y (m)	-8.28E-3	-1.04E-2	25.6	3.20E-3	3.86E-3	20.6	0.00E+0	0.00E+0	-
U_Z (m)	0.00E+0	0.00E+0	-	0.00E+0	0.00E+0	-	1.53E+0	1.52E+0	-0.6
R_X (deg)	0.00E+0	0.00E+0	-	0.00E+0	0.00E+0	-	7.57E+0	7.53E+0	-0.6
R_Y (deg)	0.00E+0	0.00E+0	-	0.00E+0	0.00E+0	-	1.29E+0	1.36E+0	4.9
R_Z (deg)	-3.98E+0	-3.97E+0	-0.3	4.47E-2	4.30E-2	-3.8	0.00E+0	0.00E+0	-
	M_X=1.0E6Nm			M_Y=1.0E6Nm			M_Z=1.0E6Nm		
	GFEM	Beam	Δ(%)	GFEM	Beam	Δ(%)	GFEM	Beam	Δ(%)
U_X (m)	0.00E+0	0.00E+0	-	0.00E+0	0.00E+0	-	-6.94E-2	-6.92E-2	-0.3
U_Y (m)	0.00E+0	0.00E+0	-	0.00E+0	0.00E+0	-	7.83E-4	7.51E-4	-4.1
U_Z (m)	1.32E-1	1.31E-1	-0.6	2.26E-2	2.36E-2	4.8	0.00E+0	0.00E+0	-
R_X (deg)	9.08E-1	9.08E-1	-	2.14E-1	2.14E-1	0.1	1.00E-6	1.00E-6	-
R_Y (deg)	2.14E-1	2.14E-1	0.1	2.48E+0	2.49E+0	0.1	1.00E-6	1.00E-6	-
R_Z (deg)	1.00E-6	1.00E-6	-	1.00E-6	1.00E-6	-	4.85E-1	4.85E-1	-

appears too flexible in tension. This error is probably negligible for practical applications as the wing is unlikely to experience significant loading or displacements in the spanwise direction. In any case, the bending, twist and shear deflections, due to applied bending moments (M_X,M_Z), torques (M_Y) and shear forces (F_X,F_Z), are likely to be orders of magnitude larger than the extension or shear-extension coupling deflections.

From an MDO point of view, the tip deflection trends with model updates are also of interest. To illustrate these trends in more detail, the model 1 and 2 updates were performed in smaller increments, corresponding to the intermediary points in Fig. 12 and 13. Clearly, for the shear load (F_Z) case, the displacement and rotation trends are captured with sufficient accuracy for MDO purposes. Interestingly, the trends are also captured correctly for the applied spanwise force (F_Y), despite the deflection magnitude error increasing with increasing bend-twist coupling.

B. Representative GFEM of a high-aspect-ratio wing

The University of Bristol Ultra-Green (BUG) cantilevered wing design was inspired by the strut-supported high-aspect-ratio wing of the NASA SUGAR Volt aircraft configuration [30], with the main aim of studying the nonlinear aeroelastic effects associated with large wing deflections [9, 31, 32]. The BUG half-wing FEM model (48564 degrees of freedom) has a span of 25.89m and is shown in Fig. 14. The beam reference axis is defined at half-chord and consists of 3 straight reference axis sections. The level of complexity included in the wing-box is comparable to that of models used for conceptual design studies in industry; it has a non-rectangular cross-section, with varying sweep and taper along the span, and internal ribs with varying orientations. L-section stringers, parallel to the front spar and with section property h tapering from 59mm at the root to 16mm at the tip, are modeled on the wing skins using beam elements. The

skin, stringer, spar and rib material properties are listed in Table 3. The BUG GFEM (and reduced beam model) input files are published in reference [33] to allow independent model analysis and verification. Bend-twist coupling was introduced in the GFEM model by defining anisotropic material properties in the skins, representative of a homogenized 0°/±45°/90° ply composite laminate, with fixed ply ratios of 60%, 30% and 10% respectively, and where the 0° ply angle was rotated forward of the front spar direction by 26°.

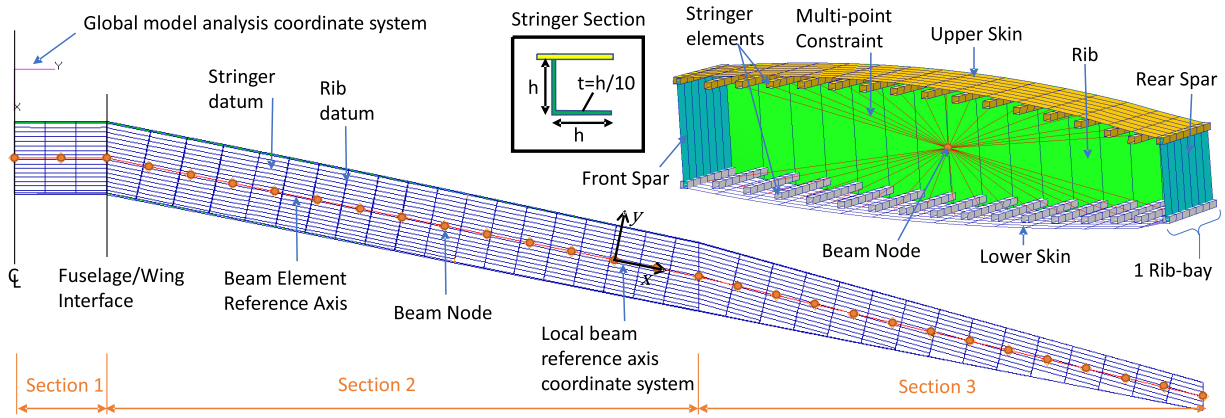

Fig. 14 Half-wing GFEM model structural layout (bottom) and detailed mesh of a representative rib-bay section (top-right)

Table 3 Material properties for the isotropic ribs, spars and stringers (A) and composite skin plies (B)

	E_1 (GPa)	E_2 (GPa)	G_{12} (GPa)	ν_{12}	$\rho\ (kg/m^3)$
Material A	72.4	72.4	27.3	0.33	1578
Material B	128.0	11.0	4.5	0.28	1520

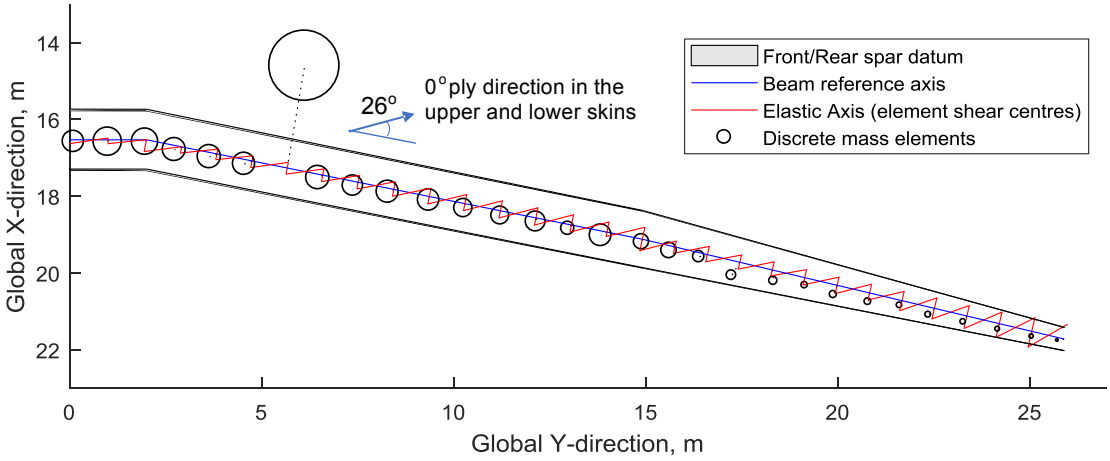

Fig. 15 Equivalent beam model elastic axis and discrete mass element CG locations (circle size is indicative of the relative mass in kg)

The BUG GFEM model was reduced to an equivalent beam model using the stiffness and mass reduction methods

described in sections III and IV. So as to remove the effect of the load introduction assumptions on the equivalent stiffness parameter calculations at the tip of wing sections 1 and 2 (see section A), the forces and moments used for the stiffness reduction were applied at the wingtip for all wing sections. The moments generated at the tip of sections 1 and 2 by the wing-tip forces $F_{1,2,3}$ are easily determined from the wing geometry and their effect on the wing deflection is negated by applying the inverse moments at the wingtip, in addition to $F_{1,2,3}$. The equivalent beam model elastic axis, mass distribution and the beam stiffness properties are plotted in figures 15 and 16. The thickness distributions are equal on the upper and lower skins and on the front and rear spars in the GFEM model, so that the average shear center offset from the beam reference axis over each element is close to zero. The lumped mass element CG locations are generally close to the beam reference axis, except for the element including the engine mass, which is offset forward and down of the reference beam node by 2.7m and 1.1m respectively.

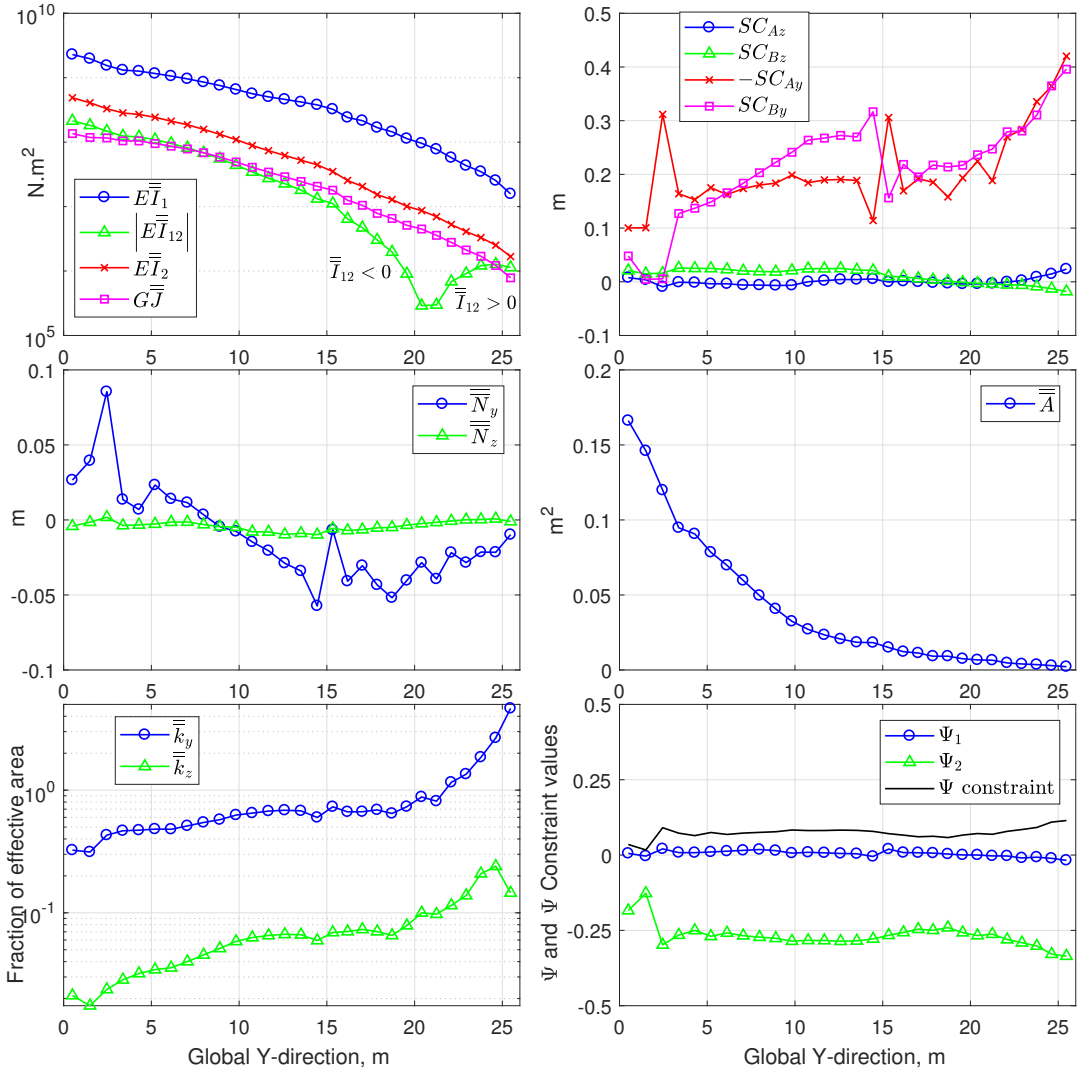

Fig. 16 Equivalent beam model stiffness parameters along the wing span

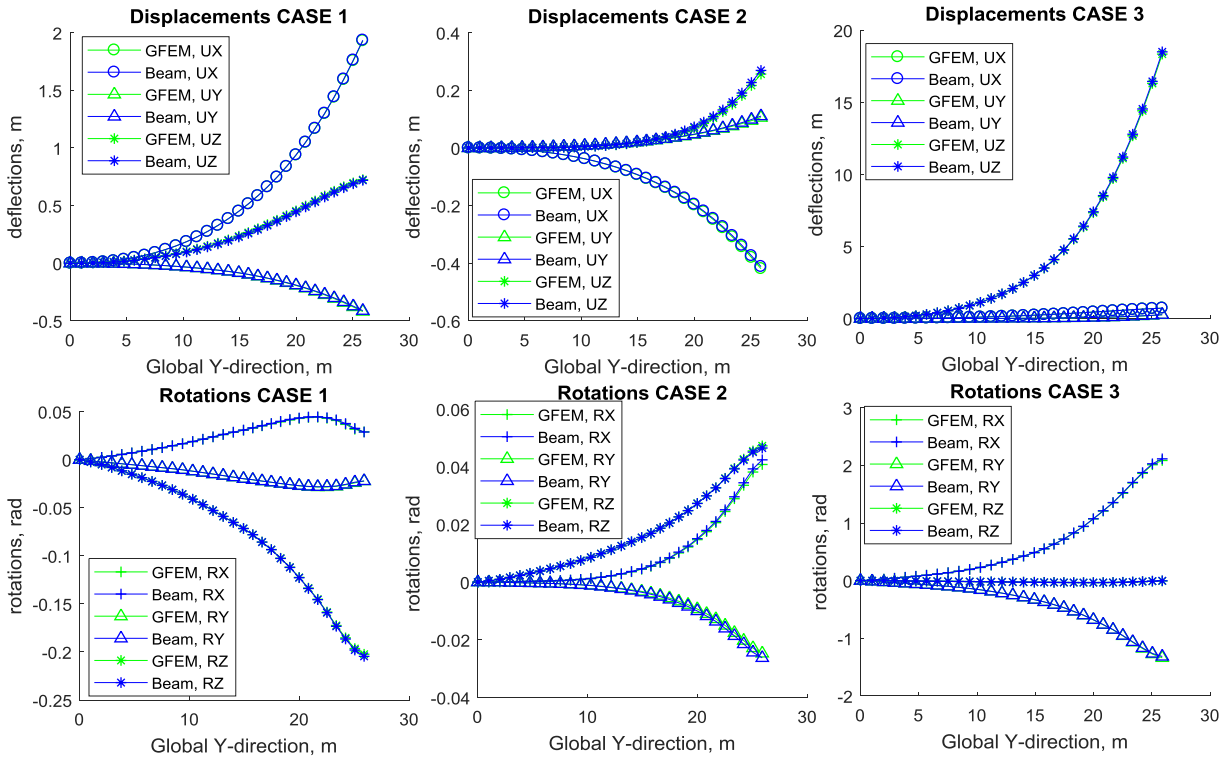

Fig. 17 Comparison of the GFEM and equivalent beam displacements and rotations due to tip forces of: $F_X = 2.10^5$N (Case 1), $F_Y = 2.10^5$N (Case 2), $F_Z = 2.10^5$N (Case 3)

Table 4 Comparison of the GFEM and equivalent beam first 10 normal mode frequencies

		Natural Frequencies (Hz)		
Mode number	GFEM Mode Shape	GFEM	Beam model	Error (%)
1	1st Z-bending	1.26	1.26	-0.1
2	2nd Z-bending	3.00	3.03	1.0
3	1st X-bending	3.18	3.18	0.1
4	3rd Z-bending	3.65	3.69	1.1
5	4th Z-bending	6.71	6.76	0.7
6	2nd X-bending	9.48	9.37	-1.1
7	5th Z-bending	11.23	11.27	0.4
8	torsion mode	14.71	14.78	0.5
9	6th Z-bending	15.96	16.30	2.1
10	3rd X-bending	17.54	17.48	-0.4

The GFEM and equivalent beam model wing deflections along the span are compared for 3 static linear wingtip load cases, where a 2.10^5N force is successively applied in the global coordinate system X-Y-Z directions at the tip node (Cases 1, 2 and 3 respectively). The resulting node displacements and rotations in and about the global coordinate system directions are plotted in figure 17. The maximum wingtip displacement error of the equivalent beam with respect to the GFEM, is of 5% (U2 for Case 2) and there is an overall good correlation along the wing span for all

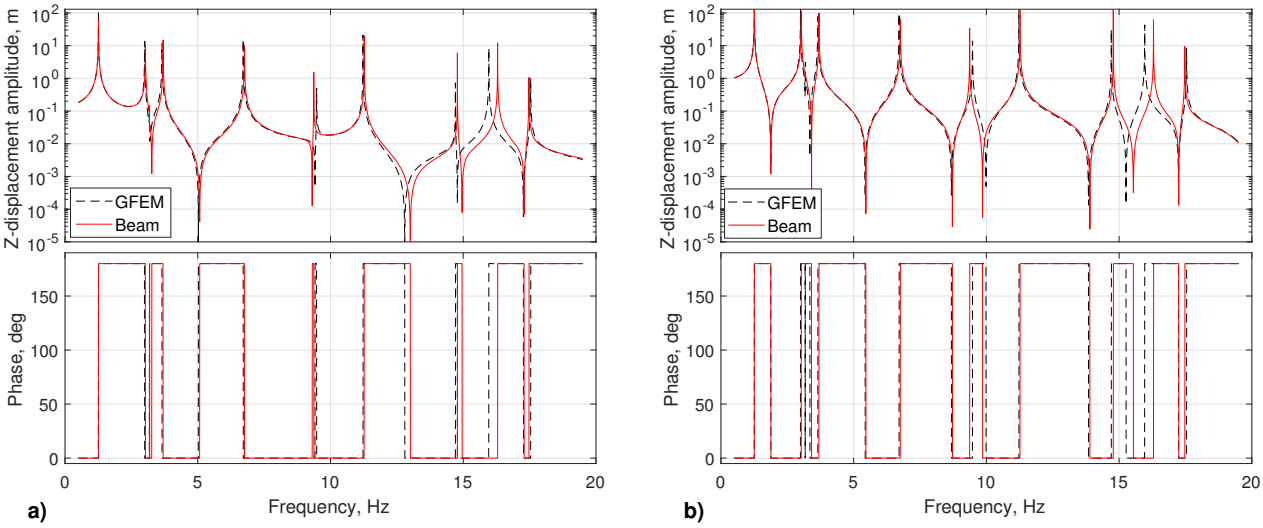

Fig. 18 Frequency response plots at two spanwise wing positions, Y=14.9m (a) and Y=25.9m (b), for an applied wing tip excitation force of 1.10^4N in the Global Z-direction

displacements and rotations.

Next, an eigenvalue analysis is performed on the GFEM and on the beam model and the first 10 natural frequencies are compared in Table 4, showing a very good correlation between the full GFEM and the equivalent beam model. Mode shape descriptions relate to the dominant deflections, since bending and torsion deflections are coupled. The maximum relative error of 2.1%, encountered for the ninth mode, is considered to be well within the interval of uncertainty of any practical application of this approach for either loads calculation or stability analysis.

Finally, the frequency response of the equivalent beam model is compared to the full GFEM model. For brevity, only the frequency response functions for a Z-direction tip force excitation are shown in Fig. 18 for two spanwise stations, at Y=14.9m and Y=25.9m, respectively. The first station corresponds to the "misaligned" rib at the end of the wing's Section 2 (see Fig. 14) marking the transition to the region of chord taper in the outer box. The second station corresponds to the wing tip. No damping has been included in the models, as evidenced by the phase angle taking only values of $0\,^\circ$ or $180\,^\circ$. As for the comparison of the natural frequencies, the models display excellent correlation across the whole frequency range examined. It should be noted that the contribution of the third mode (1st X-bending), albeit small given that the excitation is primarily exciting Z-bending, is visible for both models. It must be mentioned here, that the idealization of the engine attachment considered lends itself well to an analysis of the BUG wing box with beam theory. More complex engine attachments may potentially introduce local structural complexity that could lead to local structural dynamics difficult to capture with beam idealizations of the wingbox.

VI. Gradient data extraction method

As discussed in section II, the sensitivities of the beam element properties and the mass matrix terms to the GFEM design variables ($\partial\Omega/\partial v$ and $\partial M/\partial v$) have to be calculated for gradient based aeroelastic optimization. The present beam reduction method has the advantage of readily yielding the sensitivities of the stiffness parameters for each beam element as

$$\frac{\partial \Omega}{\partial v} = \frac{\partial \Omega}{\partial C}\,\frac{\partial C}{\partial U}\,\frac{\partial U}{\partial v}\,, \tag{25}$$

where $\partial\Omega/\partial C$ is the (13x36) Jacobian matrix of the beam element sensitivities to the terms of the flexibility matrix $[C]$ from section III and $\partial U/\partial v$ are the sensitivities of the reference node deflections due to changes in the GFEM variables, such as changes in the wing spar or skin thickness or composite ply percentages. The matrix $\partial U/\partial v$ is a standard output of MSC Nastran SOL200 and it is determined from the stiffness relation between the applied force vector F, the stiffness matrix K and the nodal displacement and rotation vector U as

$$F = KU \Rightarrow \frac{\partial U}{\partial v}K = \frac{\partial F}{\partial v} - \frac{\partial K}{\partial v}U. \tag{26}$$

In this equation, $\partial F/\partial v = 0$ for the static wing tip load cases used for the stiffness reduction, $\partial K/\partial v$ is calculated analytically or by finite differences depending on the GFEM property/variable relationship, and K and U are available from the static finite element solution.

In equation (25), the matrices $\partial\Omega/\partial C$ and $\partial C/\partial U$ can be determined by analytically differentiating the equations from section III and chain-ruling the resulting terms. For example, from equations (5) and (6), the shear center location at node B is a function of the rotated flexibility matrix $\bar{C}$ and of transformation matrix T, which is a function of the Euler rotation angles γ_z and γ'_y. The sensitivity of the shear center location SC_{By} to changes in the reference node deflections, may then be found from

$$\frac{\partial SC_{By}}{\partial U} = \frac{\partial SC_{By}}{\partial \bar{C}}\left(\frac{\partial \bar{C}}{\partial C}\,\frac{\partial C}{\partial U} + \frac{\partial \bar{C}}{\partial \gamma_{y'}}\,\frac{\partial \gamma'_y}{\partial U} + \frac{\partial \bar{C}}{\partial \gamma_z}\,\frac{\partial \gamma_z}{\partial U}\right) + \frac{\partial SC_{By}}{\partial \gamma'_y}\,\frac{\partial \gamma'_y}{\partial U} + \frac{\partial SC_{By}}{\partial \gamma_z}\,\frac{\partial \gamma_z}{\partial U}. \tag{27}$$

All terms, except $\partial\gamma'_y/\partial U$ and $\partial\gamma_z/\partial U$, can be derived directly from equations (1) to (6). Furthermore, a residual-based solution approach ([34]) can be used to determine the two remaining unknown partial derivatives $\partial\gamma'_y/\partial U$ and $\partial\gamma_z/\partial U$.

Using this approach, we define the function array $f = [\bar{C}_{45}; \bar{C}_{46}] = [0; 0]$ for any U, so that

$$\frac{\partial f}{\partial U} = 0 = \frac{\partial f}{\partial C}\frac{\partial C}{\partial U} + \frac{\partial f}{\partial \gamma}\frac{\partial \gamma}{\partial U} \quad \Rightarrow \quad \frac{\partial \gamma}{\partial U} = \left[\frac{\partial f}{\partial \gamma}\right]^{-1}\left(-\frac{\partial f}{\partial C}\frac{\partial C}{\partial U}\right), \tag{28}$$

$$\text{with } \frac{\partial \gamma}{\partial U} = \begin{bmatrix} \partial \gamma_y'/\partial U \\ \partial \gamma_z/\partial U \end{bmatrix} \quad \text{and} \quad \frac{\partial f}{\partial \gamma} = \begin{bmatrix} \partial \bar{C}_{45}/\partial \gamma_y' & \partial \bar{C}_{45}/\partial \gamma_z \\ \partial \bar{C}_{46}/\partial \gamma_y' & \partial \bar{C}_{46}/\partial \gamma_z \end{bmatrix} \text{ nonsingular.}$$

It is assumed that the system from equation (4) has already been solved, yielding the rotation angles γ_y' and γ_z, so that these terms can be back-substituted into this equation to determine $\partial f/\partial \gamma$ and $\partial f/\partial C$. The other stiffness parameter gradients $\partial \Omega/\partial U$ may be found in a similar way.

Finally, the lumped mass matrix $[M]$ sensitivities to changes in the GFEM variables are available as a by-product of the mass reduction process. These gradients are calculated as

$$\frac{\partial [M]}{\partial v} = \sum_{i=1}^{n} \frac{\partial [M]}{\partial m_i}\frac{\partial m_i}{\partial v} \tag{29}$$

where $\partial [M]/\partial m_i$ is calculated from equations (23) and (24) and $\partial m_i/\partial v$ is defined by the GFEM element property dependence on the design variables.

VII. Gradient data example

The method from section VI is implemented for the constant-section rectangular wing-box from section A, to analytically extract the beam stiffness parameter sensitivities to changes in the +45° fiber percentage in the upper skin. These sensitivities are evaluated with respect to the baseline and model 3 configurations and results are plotted in figure 19. Approximate sensitivities are first determined using a forward finite difference approach applied to the GFEM. A step size of 0.7% of +45° fibers is used, which corresponds to a 2% increment over a design range of 4% to 40% of +45° fibers. This step size was found to yield a good approximation of the gradients, with truncation and condition errors being small. The finite difference gradients are plotted on top of the analytical data in figure 19, showing a good correlation with the analytical data and therefore verifying the method from section VI. The analytical gradients are then also compared locally with gradients calculated using a complex-step derivative approximation ([35]), which yields more accurate gradient estimates than the finite difference approximation. The $\partial \Omega/\partial U$ terms from equation (25) are calculated using this approach and multiplied with the $\partial U/\partial v$ obtained from the GFEM solution, since it is not currently possible to input a complex property step in MSC Nastran. The relative error of the complex-step gradient approximations for an element at mid-span (Y=8.1m) on model 3 is plotted in figure 20 for two different complex step sizes h, where $\partial \Omega/\partial U \approx \text{Im}\left[\Omega(U + ih)\right]/h$. The relative error for all beam properties is shown to converge to $\epsilon \leq 10^{-5}$ for $h \leq 10^{-7}$.

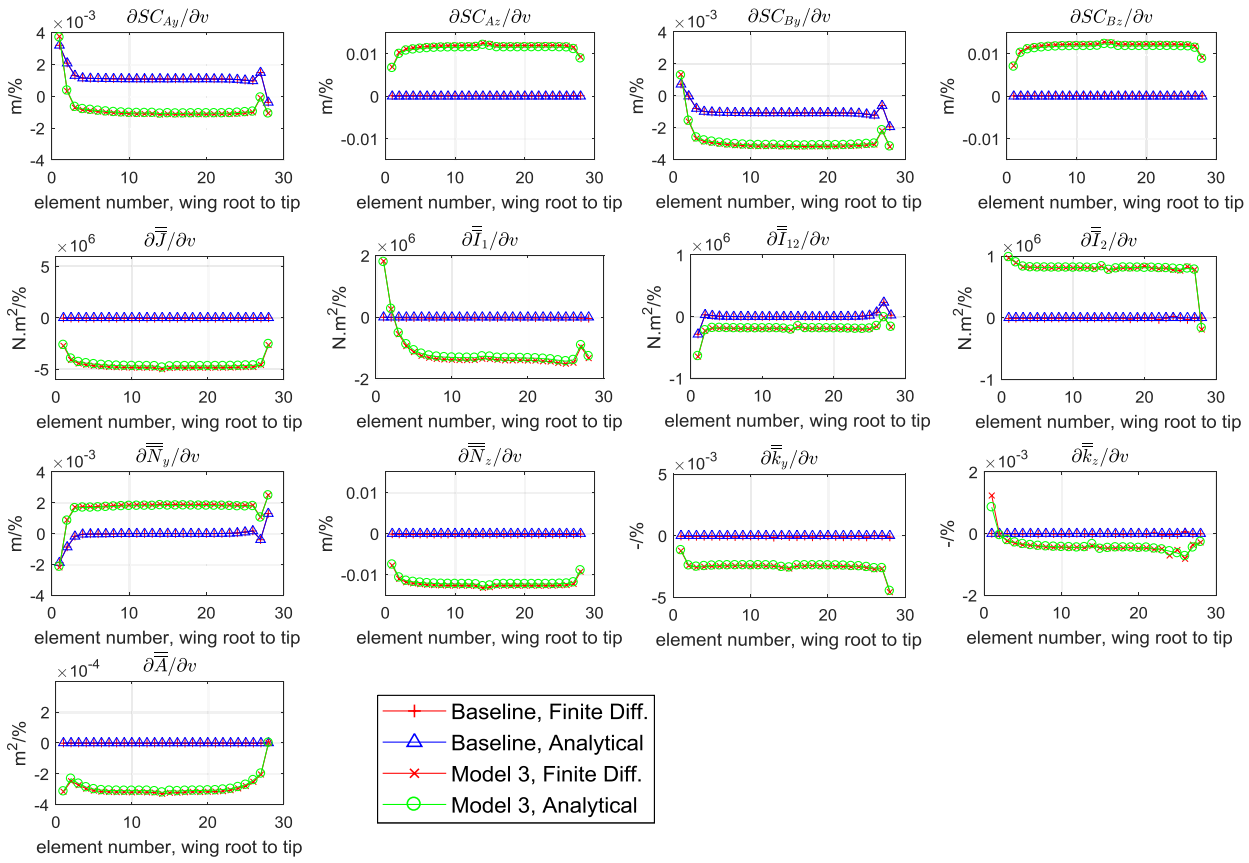

Fig. 19 Beam stiffness parameter sensitivities to changes in the +45° fiber percentage in the upper skin

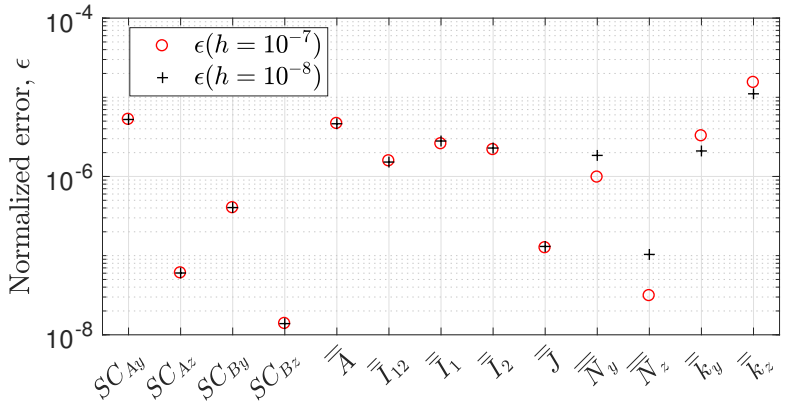

Fig. 20 Relative error of the complex-step derivative approximations $f' = \partial\Omega/\partial v$ with respect to the analytic results for Model 3, calculated as $\epsilon = |f' - f'_{ref}|/|f'_{ref}|$

In figure 19, for the baseline model, only the shear center and neutral axis offsets in the y-direction (SC_{Ay}, SC_{By}, $\bar{\bar{N}}_y$) and the bending stiffness parameter $\bar{\bar{I}}_{12}$ have any noticeable sensitivity to the change in the ply percentage. Towards the wing mid-span, the main effect of increasing the percentage of +45° fibers in the upper skin is to induce a rotation of the beam element elastic axis about the z-direction ($\gamma_z < 0$), so that SC_{Ay} increases and SC_{By} decreases by the same

amount ($\partial SC_{Ay}/\partial v > 0, \partial SC_{By}/\partial v < 0$). Towards the wing root, SC_{Ay} increases further and SC_{By} also increases with $\partial SC_{By}/\partial v > 0$ at the wing root, still indicating a rotation of the beam element elastic axis about the z-direction, but also a shift forward, in the positive y-direction. This behavior corresponds to an effective stiffening of the front-spar region towards the wing root. The opposite effect can be seen towards the wing tip, where the average shear center is shifted aft.

The beam stiffness parameter sensitivities for model 3 can also be compared with the baseline model sensitivities. For model 3, an increase in the +45° fiber percentage in the upper skin not only affects all the beam stiffness parameters that were insensitive to this variable on the baseline model, but the shear center sensitivities are also clearly different from the baseline sensitivities. Away from the wing root, $\partial SC_{Ay}/\partial v$ and $\partial SC_{By}/\partial v$ for model 3 are offset by approximately -2mm/% relative to the baseline model sensitivities, so that the rotation of the elastic axis about the z-direction due to an increase in the +45° fiber percentage is similar for both models, but with an additional shift aft of the elastic axis for model 3. Indeed, this tendency of the average shear center location $\overline{SC_y}$ to move aft for an increase in the +45° fiber percentage was already apparent in the transition from model 1 to model 2, where $\overline{SC_y}$ was 0.1m for model 1 and 0.08m for model 2 (see table 1 and figures 10 and 11). Moreover, since $\partial SC_{Az}/\partial v > 0$ and $\partial SC_{Bz}/\partial v > 0$ for model 3, the upper skin is effectively stiffened by increasing its +45° fiber percentage.

This example demonstrates the robustness of the reduction method for generating gradients. It also shows that changes in composite laminate ply percentages can have non-intuitive effects on the wing stiffness properties, even for an apparently simple wing geometry, and that these effects are very dependent on the stiffness properties of the reference wing structure. These facts clearly indicate that, in order to design a wing with certain stiffness properties and in particular with bend-twist coupling, a formal optimization process should be used.

VIII. Conclusions

In this work, a numerical method was presented for efficiently and accurately reducing a high-fidelity wing GFEM to a Timoshenko beam theory model with lumped masses. An approach has been suggested for integrating the beam reduction method into a gradient-based aeroelastic design optimization architecture, so as to improve the efficiency and scope of existing aeroelastic design optimization implementations.

The beam reduction method, which results in 13 independent physical beam stiffness parameters per element and also yields sensitivity information with respect to changes in the GFEM, was first demonstrated on a simplified wing-box and then on the University of Bristol Ultra-Green aircraft configuration wing. The calculated equivalent beam stiffness and mass properties were verified by comparing the GFEM and beam model behaviors, both statically and dynamically. The beam models were shown to capture the GFEM bending and torsion behaviors accurately, with static deflection errors below 5% and a maximum natural frequency error of 2.1% for the first 10 modes. Larger errors may occur for deflections along the beam axis, since extension-shear coupling effects cannot be fully captured by the 13 beam stiffness parameters. The analytical beam model gradients were verified with respect to gradients estimated using a finite

difference approach on the GFEM. Again, an excellent correlation was found between the beam and GFEM gradients for different reference models.

It was shown that the reduction method has the ability to give insight into the GFEM design optimization results, by relating the properties of high-fidelity variable section, anisotropic wings to isotropic beam properties, such as the location of the elastic axis along the span. Non-dimensional bend-twist coupling parameters can be evaluated to allow insight into the aeroelastic behavior of a wing. The beam model gradients provide information about the effects that potential design changes may have on the overall wing stiffness and mass properties, in the vicinity of the current design solution. These effects may not be intuitive, particularly where composite wings or wings with significant bend-twist coupling are considered.

Acknowledgments

The authors would like to acknowledge the support of Innovate UK for funding the research under the Agile Wing Integration project. In addition, J.E. Cooper holds a Royal Academy of Engineering Research Chair and S.A. Neild is supported by the Engineering and Physical Sciences Research Council (EPSRC) fellowship EP/K005375/1.

References

[1] Daoud, F., Deinert, S., and Bronny, P., "Multidisciplinary Airframe Design Process : Incorporation of steady and unsteady aeroelastic loads," *12th AIAA ATIO Conference and 14th AIAA/ISSMO Multidisciplinary Analysis and Optimization Conference*, Indianapolis, Indiana, 2012. URL https://doi.org/10.2514/6.2012-5715.

[2] Stanford, B., and Dunning, P., "Optimal Topology of Aircraft Rib and Spar Structures under Aeroelastic Loads," *10th AIAA Multidisciplinary Design Optimization Conference*, National Harbor, Maryland, 2014. URL https://doi.org/10.2514/6.2014-0633.

[3] Stanford, B. K., Jutte, C. V., and Wieseman, C. D., "Trim and Structural Optimization of Subsonic Transport Wings Using Nonconventional Aeroelastic Tailoring," *AIAA Journal*, Vol. 54, No. 1, 2016, pp. 293–309. URL https://doi.org/10.2514/1.J054244.

[4] Stodieck, O., Cooper, J. E., Weaver, P. M., and Kealy, P., "Aeroelastic tailoring of a representative wing box using tow-steered composites," *AIAA Journal*, Vol. 55, No. 4, 2017, pp. 1425–1439. URL https://doi.org/10.2514/1.J055364.

[5] Brooks, T. R., Kennedy, G., and Martins, J., "High-fidelity Multipoint Aerostructural Optimization of a High Aspect Ratio Tow-steered Composite Wing," *58th AIAA/ASCE/AHS/ASC Structures, Structural Dynamics, and Materials Conference*, Grapevine, Texas, 2017. URL https://doi.org/10.2514/6.2017-1350.

[6] Francois, G., Cooper, J. E., and Weaver, P. M., "Aeroelastic tailoring using the spars and stringers planform geometry," *58th AIAA/ASCE/AHS/ASC Structures, Structural Dynamics, and Materials Conference*, Grapevine, Texas, 2017. URL https://doi.org/10.2514/6.2017-1360.

[7] Khodparast, H. H., Georgiou, G., Cooper, J. E., Ricci, S., Vio, G. A., and Denner, P., "Efficient Worst Case "1-Cosine" Gust Loads Prediction," *ASDJournal*, Vol. 2, No. 3, 2012, pp. 33–54. URL https://doi.org/10.3293/asdj.2012.17.

[8] Su, W., and S. Cesnik, C. E., "Dynamic Response of Highly Flexible Flying Wings," *AIAA Journal*, Vol. 49, No. 2, 2011, pp. 324–339. URL https://doi.org/10.2514/1.J050496.

[9] Howcroft, C., Calderon, D., Lambert, L., Castellani, M., Cooper, J. E., Lowenberg, M. H., and Neild, S., "Aeroelastic Modelling of Highly Flexible Wings," *15th Dynamics Specialists Conference*, San Diego, California, 2016. URL https://doi.org/10.2514/6.2016-1798.

[10] Yu, W., Volovoi, V. V., Hodges, D. H., and Hong, X., "Validation of the Variational Asymptotic Beam Sectional Analysis," *AIAA Journal*, Vol. 40, No. 10, 2002, pp. 2105–2112. URL https://doi.org/10.2514/2.1545.

[11] Volovoi, V. V., Hodges, D. H., Cesnik, C. E., and Popescu, B., "Assessment of beam modeling methods for rotor blade applications," *Mathematical and Computer Modelling*, Vol. 33, No. 10-11, 2001, pp. 1099–1112. URL https://doi.org/10.1016/S0895-7177(00)00302-2.

[12] Librescu, L., and Song, O., *Thin-walled composite beams: theory and application*, Solid Mechanics and Its Applications, Vol. 131, Springer, 2006.

[13] Carrera, E., and Petrolo, M., "Refined One-Dimensional Formulations for Laminated Structure Analysis," *AIAA Journal*, Vol. 50, No. 1, 2012, pp. 176–189. URL http://dx.doi.org/10.2514/1.J051219.

[14] Hu, P., Yu, W., Hodges, D. H., and Ku, J., "VABS-IDE: VABS-Enabled Integrated Design Environment (IDE) for Efficient High-Fidelity Composite Rotor Blade and Wing Design," *51st AIAA/ASME/ASCE/AHS/ASC Structures, Structural Dynamics, and Materials Conference*, Orlando, Florida, 2010. URL https://doi.org/10.2514/6.2010-3063.

[15] De Breuker, R., Abdalla, M., Werter, N., Vandewaeter, L., Ferede, E., Dillinger, J., and Kruger, W., "An Aeroelastic Multi-Fidelity Approach for Aeroelastic Tailoring," *Proceedings of the International forum on Aeroelasticity and Structural Dynamics*, Royal Aeronautical Society, Bristol, United Kingdom, 2013.

[16] Yu, W., "A Unified Theory for Constitutive Modeling of Composites," *Journal of Mechanics of Materials and Structures*, Vol. 11, No. 4, 2016, pp. 379–411. doi:10.2140/jomms.2016.11.379, URL https://doi.org/10.2140/jomms.2016.11.379.

[17] Malcolm, D. J., and Laird, D. L., "Extraction of equivalent beam properties from blade models," *Wind Energy*, Vol. 10, No. 2, 2007, pp. 135–157. URL https://doi.org/10.1002/we.213.

[18] Martins, J. R. R. A., and Lambe, A. B., "Multidisciplinary Design Optimization: A Survey of Architectures," *AIAA Journal*, Vol. 51, No. 9, 2013, pp. 2049–2075. URL https://doi.org/10.2514/1.J051895.

[19] Martins, J. R. R. A., and Hwang, J. T., "Review and Unification of Methods for Computing Derivatives of Multidisciplinary Computational Models," *AIAA Journal*, Vol. 51, No. 11, 2013, pp. 2582–2599. URL http://dx.doi.org/10.2514/1.J052184.

[20] Chen, H., Yu, W., and Capellaro, M., "A critical assessment of computer tools for calculating composite wind turbine blade properties," *Wind Energy*, Vol. 13, No. 6, 2009, pp. 497–516. URL https://doi.org/10.1002/we.372.

[21] Resor, B., Paquette, J., Laird, D., and Griffith, T., "An Evaluation of Wind Turbine Blade Cross Section Analysis Techniques," *51st AIAA/ASME/ASCE/AHS/ASC Structures, Structural Dynamics, and Materials Conference*, Orlando, Florida, 2010. URL https://doi.org/10.2514/6.2010-2575.

[22] Resor, B., and Paquette, J., "Uncertainties in Prediction of Wind Turbine Blade Flutter," *52nd AIAA/ASME/ASCE/AHS/ASC Structures, Structural Dynamics and Materials Conference*, Denver, Colorado, 2011. URL https://doi.org/10.2514/6.2011-1947.

[23] Branner, K., Blasques, J., Kim, T., Fedorov, V., Berring, P., Bitsche, R., and Berggreen, C., *Anisotropic beam model for analysis and design of passive controlled wind turbine blades*, DTU Wind Energy, Report (DTU Wind Energy E; No. 0001), Denmark, 2012.

[24] Saravia, M. C., Saravia, L. J., and Cortínez, V. H., "A one dimensional discrete approach for the determination of the cross sectional properties of composite rotor blades," *Renewable Energy*, Vol. 80, No. Supplement C, 2015, pp. 713–723. URL https://doi.org/10.1016/j.renene.2015.02.046.

[25] Rafiee, R., Moradi, M., and Khanpour, M., "The influence of material properties on the aeroelastic behavior of a composite wind turbine blade," *Journal of Renewable and Sustainable Energy*, Vol. 8, 2016, pp. 063305–1–12. URL https://doi.org/10.1063/1.4968600.

[26] Rehfield, L. W., and Atilgan, A. R., "Shear center and elastic axis and their usefulness for composite thin-walled beams," *Proceedings of the American Society of Composites, Fourth Technical Conference. Blacksburg, Virginia*, 1989, pp. 179–188.

[27] Kosmatka, J. B., "General behavior and shear center location of prismatic anisotropic beams via power series," *International Journal of Solids and Structures*, Vol. 31, No. 3, 1994, pp. 417–439. URL https://doi.org/10.1016/0020-7683(94)90114-7.

[28] Weisshaar, T. A., and Foist, B. L., "Vibration tailoring of advanced composite lifting surfaces," *Journal of Aircraft*, Vol. 22, No. 2, 1985, pp. 141–147. URL https://doi.org/10.2514/3.45098.

[29] *Matlab R2017b documentation*, MathWorks, Optimization Toolbox > Systems of Nonlinear Equations > fsolve, 2017.

[30] Bradley, M. K., Allen, T. J., and Droney, C. K., "Subsonic Ultra Green Aircraft Research: Phase II – Volume III – Truss Braced Wing Design Exploration," *NASA/CR-2015-218704, NF1676L-21006*, 2015, pp. 1–87.

[31] Cook, R. G., Calderon, D., Cooper, J. E., Lowenberg, M. H., Nield, S., and Coetzee, E., "Worst Case Gust Prediction of Highly Flexible Wings," *58th AIAA/ASCE/AHS/ASC Structures, Structural Dynamics, and Materials Conference*, Grapevine, Texas, 2017. URL https://doi.org/10.2514/6.2017-1355.

[32] Szczyglowski, C. P., Neild, S. A., Titurus, B., Jiang, J. Z., Cooper, J. E., and Coetzee, E., "Passive Gust Loads Alleviation in a Truss-Braced Wing Using Integrated Dampers," *17th International Forum on Aeroelasticity and Structural Dynamics*, Royal Aeronautical Society, Como, Italy, 2017.

[33] Stodieck, O., "BUG wing FEM models," , 2018. doi:10.5523/bris.q7lzoe14eefm2webtacs182d8, URL https://doi.org/10.5523/bris.q7lzoe14eefm2webtacs182d8.

[34] Sobieszczanski-Sobieski, J., "Sensitivity of Complex, Internally Coupled Systems," *AIAA Journal*, Vol. 28, No. 1, 1990, pp. 153–160. URL http://dx.doi.org/10.2514/3.10366.

[35] Martins, J. R., Sturdza, P., and Alonso, J. J., "The complex-step derivative approximation," *ACM Transactions on Mathematical Software (TOMS)*, Vol. 29, No. 3, 2003, pp. 245–262. URL http://dx.doi.org/10.1145/838250.838251.